

Summer 2018

Effect of Pigment Volume Concentration on Physical and Chemical Properties of Acrylic Emulsion Paints Assessed using Single-Sided Nmr

Mary Therese Rooney

College of William and Mary - Arts & Sciences, mtrooney@email.wm.edu

Follow this and additional works at: <https://scholarworks.wm.edu/etd>

 Part of the [Chemistry Commons](#)

Recommended Citation

Rooney, Mary Therese, "Effect of Pigment Volume Concentration on Physical and Chemical Properties of Acrylic Emulsion Paints Assessed using Single-Sided Nmr" (2018). *Dissertations, Theses, and Masters Projects*. Paper 1530192815.

<http://dx.doi.org/10.21220/s2-7g4k-fr37>

This Thesis is brought to you for free and open access by the Theses, Dissertations, & Master Projects at W&M ScholarWorks. It has been accepted for inclusion in Dissertations, Theses, and Masters Projects by an authorized administrator of W&M ScholarWorks. For more information, please contact scholarworks@wm.edu.

Effect of pigment volume concentration on physical and chemical properties of
acrylic emulsion paints assessed using single-sided NMR

Mary Therese Rooney

Fresh Meadows, NY

B.S. Chemistry & Mathematics, Hofstra University, 2016
B.A. Classical Literature & Languages, Hofstra University, 2016

A Thesis presented to the Graduate Faculty of
The College of William & Mary in Candidacy for the
Degree of Master of Science

Department of Chemistry

College of William & Mary
May, 2018

APPROVAL PAGE

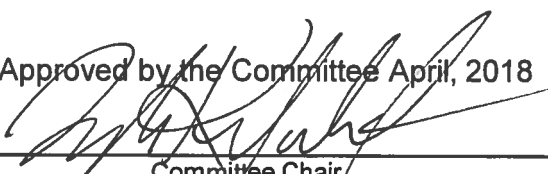
This Thesis is submitted in partial fulfillment of
the requirements for the degree of

Master of Science

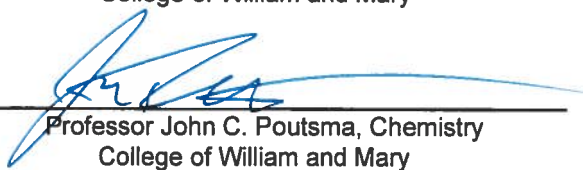


Mary Therese Rooney


Approved by the Committee April, 2018



Committee Chair
Assistant Professor Tyler K. Meldrum, Chemistry
College of William and Mary



Professor John C. Poutsma, Chemistry
College of William and Mary



Assistant Professor Nathanael M. Kidwell, Chemistry
College of William and Mary

ABSTRACT

Acrylic emulsion paint is one of the most common media employed by 20th century painters. Since early acrylic paintings have begun to require the attention of conservators, scientists are working to characterize the properties of these paints to facilitate conservation efforts. In this study, we report an investigation of the physical and chemical properties of acrylic emulsion paints using single-sided NMR in conjunction with gloss measurements and scanning electron microscopy coupled with energy dispersive spectrometry. Combining the data from these techniques gives insight into pigment-binder interactions and the acrylic curing process, showing that as pigment concentration is increased in paints, the amount of binder adsorbed to pigment particles increases, resulting in films with differing relaxation times. Furthermore, pigments with a larger surface area or smaller particle size will have a greater effect on physical properties as concentration increases. This research emphasizes the efficacy of NMR relaxometry in studying cultural heritage objects, and may prompt further study into the effects of pigment concentration on the curing and conservation of acrylic paint films.

TABLE OF CONTENTS

Acknowledgements	ii
List of Tables	iii
List of Figures	iv
Chapter 1: Introduction	1
Chapter 2: NMR Theory	5
Chapter 3: Acrylic Emulsion Paint & Pigment Volume Concentration	23
Chapter 4: Materials and Methods	31
Chapter 5: Results and Discussion	44
Chapter 6: Conclusions	58
Appendices	60
Bibliography	69

ACKNOWLEDGEMENTS

This writer wishes to express her appreciation to Professor Tyler Meldrum, under whose guidance this investigation was conducted, for his patience, guidance and criticism throughout the investigation. The author is also indebted to Professors Poutsma and Kidwell for their careful reading and criticism of the manuscript.

This writer would also like to thank the Office of Graduate Studies and Research for graduate student research grant support, as well as the College of William and Mary Graduate Studies Advisory Board for fellowship funding.

LIST OF TABLES

1. Pigment Characteristics	60
2. Sample PVCs and Λ values	61
3. T_2 data for paint films made with Golden Semi-Gloss Regular Gel Base (monoexponential fit)	62
4. T_2 data for paint films made with Golden Semi-Gloss Regular Gel Base (biexponential fit)	63
5. Comparison of T_2 data for Ivory Black and Titanium White paint films made with different acrylic bases	64

LIST OF FIGURES

1. Precession of a nuclear magnetic moment around B_0	6
2. 3D coordinate plane model of magnetization vectors	8
3. Diagram of a simple NMR experiment	13
4. Diagram of NMR-MOUSE single-sided NMR apparatus	15
5. Diagram of a Hahn echo experiment	20
6. The CPMG pulse sequence	22
7. Methyl methacrylate and n-butyl acrylate monomers	24
8. The changes in a paint film as Λ is increased	27
9. The stages in the acrylic curing process	29
10. Structures of phthalo blue and alizarin crimson	31
11. Paint being made in a fume hood	33
12. Paint sample slides	35
13. Photograph of NMR-MOUSE apparatus with sample	37
14. Profile experiment output	39
15. Fourier Transform of an echo train decay	40
16. Mono- and biexponential fit of a sample, with residuals	43
17. SEM images of ivory black paint	44
18. The change in gloss as Λ increases	45
19. Figure from [62] showing decrease in gloss	45
20. T_2 values (calculated with monoexponential fit) vs. Λ	47
21. Inverse Laplace Transforms (ILTs) of raw NMR data	48
22. Large and small T_2 values of all samples vs. Λ	49

23. SEM image of unpigmented Semi-Gloss acrylic base	51
24. Normalized amplitude of small T_2 values vs. Λ	52
25. SEM images of the four pigments	54
26. Large T_2 values of selected samples	56

Chapter 1: Introduction

Acrylic emulsion paints are the most widely used synthetic artists' paints. They were developed in the late 1950s as a versatile medium that had uniformly intense color and could be worked to produce a greater range of effects and textures than the oil paints, watercolors, and other products that had been used for centuries; their use flourished in the 1960s. The binder in acrylic emulsion paints is usually an acrylic copolymer made up of either ethyl acrylate (EA) or n-butyl acrylate (nBA) combined with methyl methacrylate (MMA) dispersed in an aqueous solution. Stabilizers, surfactants, fillers, and other materials are added to the polymer dispersion to control shelf-life and ensure optimal performance. [1–4] The aqueous base makes these paints easy to manipulate, since they can be thinned with water in order to achieve different textures, and more economical and environmentally friendly since they obviate the need for cleanup with organic solvents. [2]

Since acrylics are a relative newcomer to the art world and come in a variety of compositions, researchers are still working to characterize their properties fully, especially in regard to their degradation and reaction to conservation treatments. [5] This lack of knowledge about acrylic paints poses a problem for curators, whose duty it is to preserve (acrylic) works in museums worldwide, especially since acrylic emulsion paints are found in a large percentage of modern works. [3] Additionally, many early acrylic paintings currently need, or will soon require, the attention of conservators since it takes about half a century for buildup from air pollution to make a discernible impact on a painting's appearance. [6] Acrylic films are particularly prone to collecting dust and

pollutants due to surfactant aggregation on their soft surface, which makes the dry paint pliable and durable but also easier to soil. [6, 7]

Acrylic paint films have previously been studied with Fourier Transform infrared spectroscopy (FTIR) [7, 8, 9], x-ray fluorescence spectroscopy (XRF) [1, 10], traditional nuclear magnetic resonance spectroscopy (NMR) [11], mass spectrometry (MS) [12], and various chromatographic and microscopy techniques [5, 13– 20] which often have the unfortunate drawback of requiring a sample to be removed from the object under study. The primary instrumentation employed in this study, however, offers an attractive non-destructive alternative to these more established techniques.

Single-sided NMR, which emerged in the late 1980s and early 1990s, can non-destructively study items and chemical processes. This instrumentation improves on sensors first developed in the 1950s by scientists in the oil industry used for studying fluids trapped in rock pores in oil wells, which required the sensor to be placed inside a sample, rather than the other way around. [21] Consequently, magnets and radiofrequency coils with a flat, open geometry were developed: an “inside-out” version of the core of a traditional NMR, in which an electromagnet and coil surround a sample in a cylindrical configuration. This open geometry makes single sided NMR ideal for the study of planar samples like paint films, and eliminates the need for invasive sample removal and preparation. Therefore, it has in the past been applied to the study of cultural heritage objects like paintings [22–26], instruments [26], ceramics [27, 28], and paper [29, 30], as well as to food [31–34], manufacturing procedures [35, 36], and building materials [37].

Additionally, single-sided NMR instrumentation makes use of permanent magnets, which lessens the operation and maintenance complexity associated with traditional NMR equipment as well as the size of the instrument itself. Traditional NMR instruments use superconducting electromagnets, which require a constant replacement of cryogenics to keep the magnet operational. This renders the instruments large and immobile because of the necessary wide layers of liquid nitrogen and helium. Removing these makes single-sided NMR devices small and portable, and allows less expensive data collection than traditional high-field NMR. [38]

This streamlining of the hardware, however, comes at the cost of magnetic field strength and homogeneity. Whereas the electromagnets in traditional NMR instruments are capable of producing homogeneous fields with strengths of over twenty Tesla, the permanent magnets in the single-sided NMR instruments available in our lab produce fields on the order of half a Tesla and with a pronounced gradient. This weak, inhomogeneous field makes it impossible to collect the kind of detailed structural information about sample compounds that constitutes the most common data sets generated by traditional NMR.

Although the inhomogeneous field created by the magnets in single-sided NMR instrumentation prohibits the determination of chemical shifts and other information usually associated with a high-field NMR spectrum, spin-spin relaxation times (T_2) can be measured using the Carr-Purcell-Meiboom-Gill (CPMG) pulse sequence. [39, 40] These relaxation times correlate with the rigidity of a material; compounds like water have large T_2 values, which indicate a high level of free intermolecular motion, and smaller values of T_2 indicate restricted intermolecular motion, which, for a polymer, can

be caused by crosslinking or adsorption to a surface. [41, 42] T_2 values, however, are dependent on experimental parameters and do not provide detailed information about a material on a macroscopic level. CPMG measurements obtained using the same set of parameters can therefore be used to make comparisons across groups of samples, and data collected using other instruments is used to interpret the significance of different T_2 values.

In this study, the physical properties of acrylic emulsion paint films measured using single-sided NMR are compared to gloss and scanning electron microscopy/energy dispersive spectroscopy (SEM-EDS) measurements. Analyses were performed on paint films made with varying concentrations of four commonly used artists' pigments (ivory black, titanium white, phthalo blue, and alizarin crimson) to gain insight into the physical effects of pigmentation level on acrylic paint films. Combining the data from each technique reveals a more detailed picture of pigment-binder interactions and the acrylic curing process.

Chapter 2: NMR Theory

Nuclear magnetic resonance spectroscopy exploits the fact that most atomic nuclei possess an intrinsic angular momentum, or spin, distinct from the angular momentum that comes from the rotation of the nucleus. [43, 44] Depending upon the number of protons and neutrons that make up the nucleus (each of those subatomic particles has a spin of $\frac{1}{2}$), the nucleus itself will have a nuclear spin number, denoted I , that has a value of zero, an integer, or a half integer. Nuclei with spin number $\frac{1}{2}$ and spherical nuclear charge distribution, such as ^1H , ^{13}C , ^{15}N , and ^{31}P , are considered NMR active nuclei. Additionally, the spin state of a nucleus is degenerate, with a number of levels equal to $2I + 1$. In an applied magnetic field, the degenerate spin states in a ground state nucleus separate into different energy levels in a phenomenon known as nuclear Zeeman splitting. For nuclei with spin $\frac{1}{2}$ like ^1H , which is the only nucleus examined in this study, application of an external magnetic field results in two energy levels populated according to the Boltzmann distribution, with a few more particles in the lower energy level than in the higher level. The nuclei in the higher energy level have a quantum number of $-\frac{1}{2}$, and those in the lower energy level have a quantum number of $+\frac{1}{2}$.

Along with intrinsic angular momentum, nuclei also have an intrinsic magnetic moment, μ , and generate a small magnetic field. This magnetic moment is proportional to the nucleus' spin, with a proportionality constant, γ , called the gyromagnetic ratio. The gyromagnetic ratio of each nucleus is unique, and can be either positive or negative depending on whether the spin and magnetic moment vectors point in the same or opposite directions. If no outside forces interfere with the nuclei in a sample, these

vectors are arranged randomly and can point in any direction, resulting in a bulk magnetic moment of zero.

When these nuclei sit in an external magnetic field B_0 , however, this field interacts with the nuclear magnetic moments, causing the nucleus to precess, or rotate in a conical fashion with a constant angle around an axis in the direction of the applied magnetic field as shown in **Figure 1**.

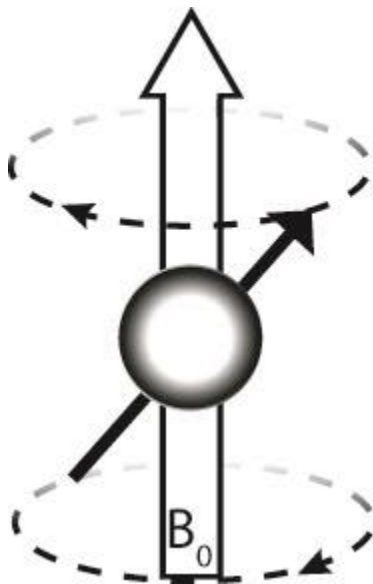


Figure 1: Precession of a single nuclear magnetic moment (solid black arrow) around an axis in the direction of an applied magnetic field. The cone described by the precessional motion will always keep the same angle between B_0 and the magnetic moment vector. The direction of the precession depends on the sign of the nucleus' gyromagnetic ratio. Nuclei with a positive γ , such as ^1H , have a negative precession like the nucleus shown in this diagram.

The frequency of the precession, called the Larmor frequency, or ω_0 , is equal to the applied magnetic field, B_0 , multiplied by the negative of the nucleus' gyromagnetic ratio:

$$\omega_0 = -\gamma B_0 \quad (2.1)$$

Over time, the thermal movement of molecules in a sample causes small fluctuations in the microscopic magnetic fields local to each nucleus generated by the magnetic moments of nearby electrons and nuclei. This fluctuation affects the precessing nuclei, gradually changing the angle of their conical motion around B_0 . The final orientation adopted by a nucleus depends on the energy of its interaction with B_0 . If a nucleus' magnetic moment is aligned perfectly with B_0 , or it is precessing in a cone with an angle of zero, the energy of the interaction between the nucleus and the applied magnetic field is very low. Therefore, in order to reach an energetically favorable configuration, the spins of the nuclei in a sample will slowly align themselves in a direction closer to the direction of B_0 until they reach equilibrium. Each individual spin vector will never exactly line up with the direction of B_0 because of the continued molecular movement in the sample and local magnetic field fluctuation which favor a more random array of spin orientations. However, the sum of all the spins in the sample, or the bulk magnetization vector, will be parallel to B_0 .

When modelling these physical phenomena to create a visual explanation for them, vectors for the applied external magnetic field, the bulk magnetization, and the individual nuclear spins are graphed on a three-dimensional coordinate plane. In this coordinate plane, shown in **Figure 2**, the vectors representing the magnetic moments of

individual nuclei in a sample all point in different directions when that sample is at equilibrium and no external magnetic field is applied. If the sample is sitting in an external magnetic field, the direction of the applied magnetic field and the bulk magnetization of the sample always line up with the z-axis when the sample is at equilibrium.

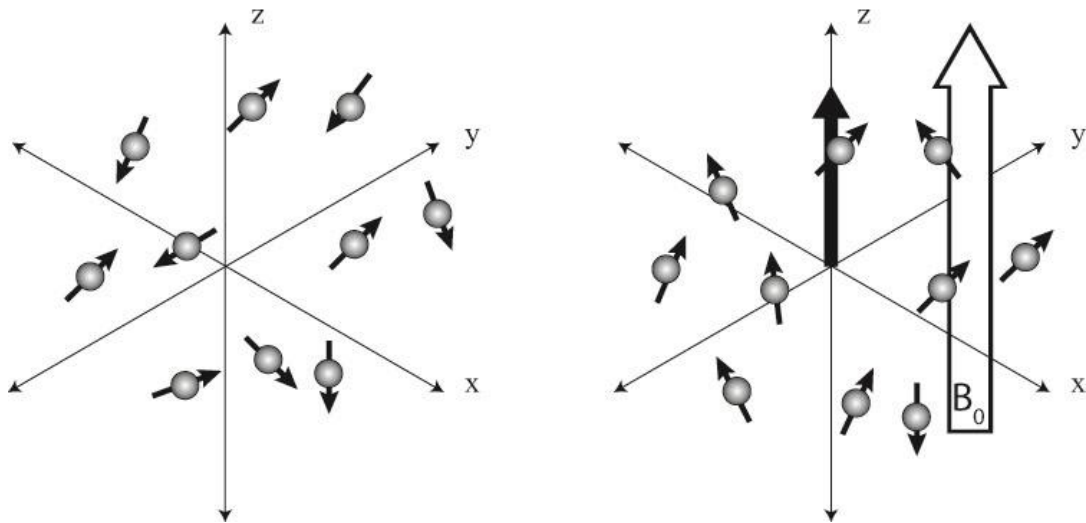


Figure 2: 3D coordinate plane model of magnetization vectors. At equilibrium, and with no external magnetic field acting on them, magnetic moment vectors of nuclei are oriented randomly and there is no net bulk magnetization (left). When a strong external magnetic field, B_0 , interacts with the individual magnetic moments, they begin to precess around B_0 and align in the direction of the field, resulting in a net bulk magnetization vector (solid black arrow) parallel to the z-axis (right).

As a result of the Zeeman splitting of spin $\frac{1}{2}$ nuclei, which dictates that the nuclei can exist in either a $+\frac{1}{2}$ or $-\frac{1}{2}$ spin state, approximately half the nuclei in a sample (those with spin $+\frac{1}{2}$) will be aligned roughly parallel to the external field and their magnetic moment vectors will point in the same direction as the applied magnetic field. The $+\frac{1}{2}$ and $-\frac{1}{2}$ spin states are also variously referred to as, respectively, the α and β states or the spin up and spin down states. The nuclei with spin $-\frac{1}{2}$, while aligned with B_0 , will have magnetic moment vectors that point in a direction opposite to the magnetic moment vector of the external field, or an anti-parallel alignment. The difference in energy between nuclei in these two states is given by the following equation:

$$\Delta E = \hbar\gamma B_0 \quad (2.2)$$

Or, substituting in **Equation 2.1**,

$$\Delta E = \hbar\omega_0 \quad (2.3)$$

where \hbar is the reduced Planck constant and γ is the gyromagnetic ratio. Therefore, the difference between the two energy levels is dependent on both the gyromagnetic ratio of the nucleus under study (42.577 MHz/Tesla for ^1H) and the strength of the applied magnetic field, and is related to the Larmor frequency of precessing nuclei in Hertz. Since the number of nuclei in a sample that populate each of the two spin states of opposite sign is almost equal, the majority of the spins cancel out each other's magnetic moment, causing the net bulk magnetization vector to take its magnitude and direction

from the spins of the small excess in population in the lower energy state, which are parallel to B_0 . The fraction of the spins that makes up this excess in population, called the polarization (p), is calculated using the equation:

$$p = \frac{N_\alpha - N_\beta}{N_\alpha + N_\beta} \quad (2.4)$$

where N_α is the number of spins parallel to B_0 and N_β is the number of spins anti parallel to B_0 .

By applying an oscillating magnetic field in the form of a radiofrequency (rf) pulse to a sample, the bulk magnetization vector can be shifted away from the direction of the applied magnetic field, or in terms of the model in **Figure 2**, away from the z-axis of the coordinate plane and towards the xy-plane. The oscillating rf field, denoted B_1 , has a much smaller magnitude than B_0 and a direction orthogonal to the direction of B_0 .

If B_1 oscillates at ω_0 , or is “on resonance”, the weak B_1 field interacts with and changes the precession of the nuclei. The easiest way to visualize the effect of B_1 on nuclear precession is to imagine the nuclei in a coordinate plane that is rotating around the z-axis at the same frequency as ω_0 . This coordinate plane is called the “rotating frame”, and within it the precessing nuclei appear to stop moving around the z-axis. Since the nuclei are now considered static with respect to their movement around B_0 , ω_0 becomes zero. Therefore, by **Equation 2.1**, the applied magnetic field B_0 that the nuclei seem to experience must also have a magnitude of zero. B_1 , though, is oscillating at the same frequency as the as the motion of the rotating frame and will therefore show up in the rotating frame system. Within the rotating frame, then, the nuclei can precess around

B_1 , rather than B_0 , with a frequency of ω_1 . As the nuclei in the sample begin to precess around B_1 , their spins start to align themselves with this new field, changing the direction of the bulk magnetic vector. The angle β between the bulk magnetization vector and the direction of B_0 caused by spin alignment to B_1 is dependent on the frequency of ω_1 and the duration, t , of the rf pulse producing B_1 :

$$\beta = \omega_1 t \quad (2.5)$$

In many NMR experiments, the duration of the rf pulse is chosen to produce a β of 90° ($\pi/2$ radians), and is usually on the order of microseconds.

This on-resonance pulse is what is used in the simplest traditional NMR experiment, shown in **Figure 3**. A sample is placed in a strong external magnetic field and allowed to equilibrate for a few seconds. After the sample's bulk magnetization aligns with the applied magnetic field, a radiofrequency coil around the sample generates a $\pi/2$ pulse, creating a new magnetic field, B_1 , aligned perpendicular to the applied magnetic field B_0 . The nuclei in the sample then begin precessing around an axis parallel to the pulse and the bulk magnetization vector shifts to the $-y$ axis. Once the pulse ends, precession resumes around the z axis. However, since the bulk magnetization vector was moved into the xy , or transverse, plane, the bulk magnetic moment is now also precessing around the z -axis. The bulk magnetization vector, then, can be broken down into two components, one parallel to the z -axis and one perpendicular (located in the xy -plane). The rotations in the xy -plane of the nucleic magnetic moments caused by this precession induce an oscillating current in the radiofrequency coil surrounding the sample that gradually tapers off as the precessing spins lose synchrony and the magnetization in the

transverse plane disappears. This current, known as the free induction decay (FID), though small, can be detected, amplified, and recorded as a digital signal. Use of a Fourier Transform can separate this signal into its various frequencies, which are then plotted to create the traditional NMR spectrum.

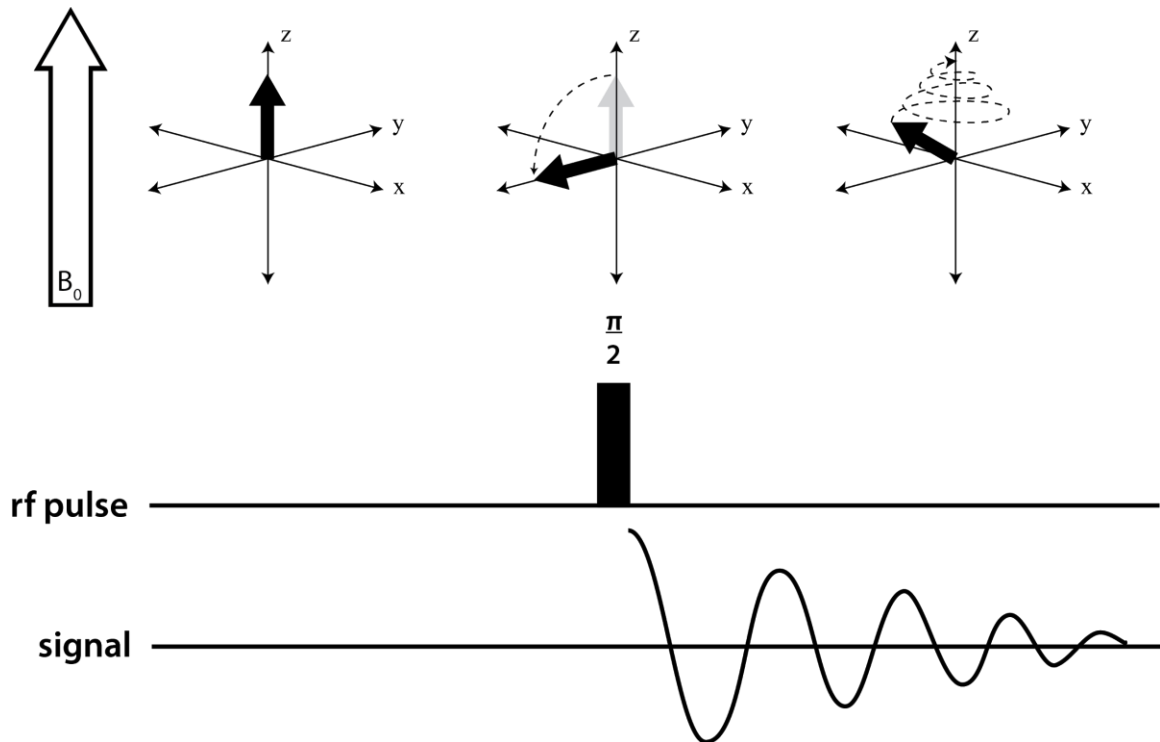


Figure 3: Diagram of a simple NMR experiment. The first set of axes shows a sample that has equilibrated in an applied magnetic field, B_0 , and has developed net magnetization in the direction of B_0 . Next, the $\pi/2$ pulse is applied, moving the net magnetization vector into the xy-plane. After the pulse ends, the net magnetization vector precesses around B_0 until it relaxes back into equilibrium; this precession in the xy-plane is detected as an oscillating current, the free induction decay, and recorded as a digital signal containing the frequencies of the precessing nuclei in the sample.

These measurements, however, require that B_0 remain homogeneous. This homogeneous B_0 is produced by a superconducting solenoid maintained with a constant electrical current, tuned with smaller magnetic shims, and wrapped in cryogenics to prevent meltdown. As mentioned in the introduction, all of this extra apparatus makes traditional NMR instrumentation bulky and static, and the geometry of the sensor limits the types of samples that it can analyze. In order to broaden the applicability of NMR to a wider array of samples, single-sided NMR devices have been developed.

In 1996, Eidmann et al. published the design of first single-sided NMR instrument, the mobile universal surface explorer or NMR-MOUSE. [45] This instrument, a version of which was employed in this study, can non-destructively analyze objects of any shape or size without requiring sample preparation, making it an attractive tool for probing the properties of a variety of materials, including fragile and irreplaceable cultural heritage objects. The NMR-MOUSE, unlike traditional high-field NMR instruments, uses permanent magnets to create the applied magnetic field B_0 . These magnets are configured in a horseshoe geometry [21], shown in **Figure 4**, with an rf coil positioned in between and aligned to their surface to allow the application of an rf field (B_1) perpendicular to B_0 and create a maximum sensitive volume for the instrument.

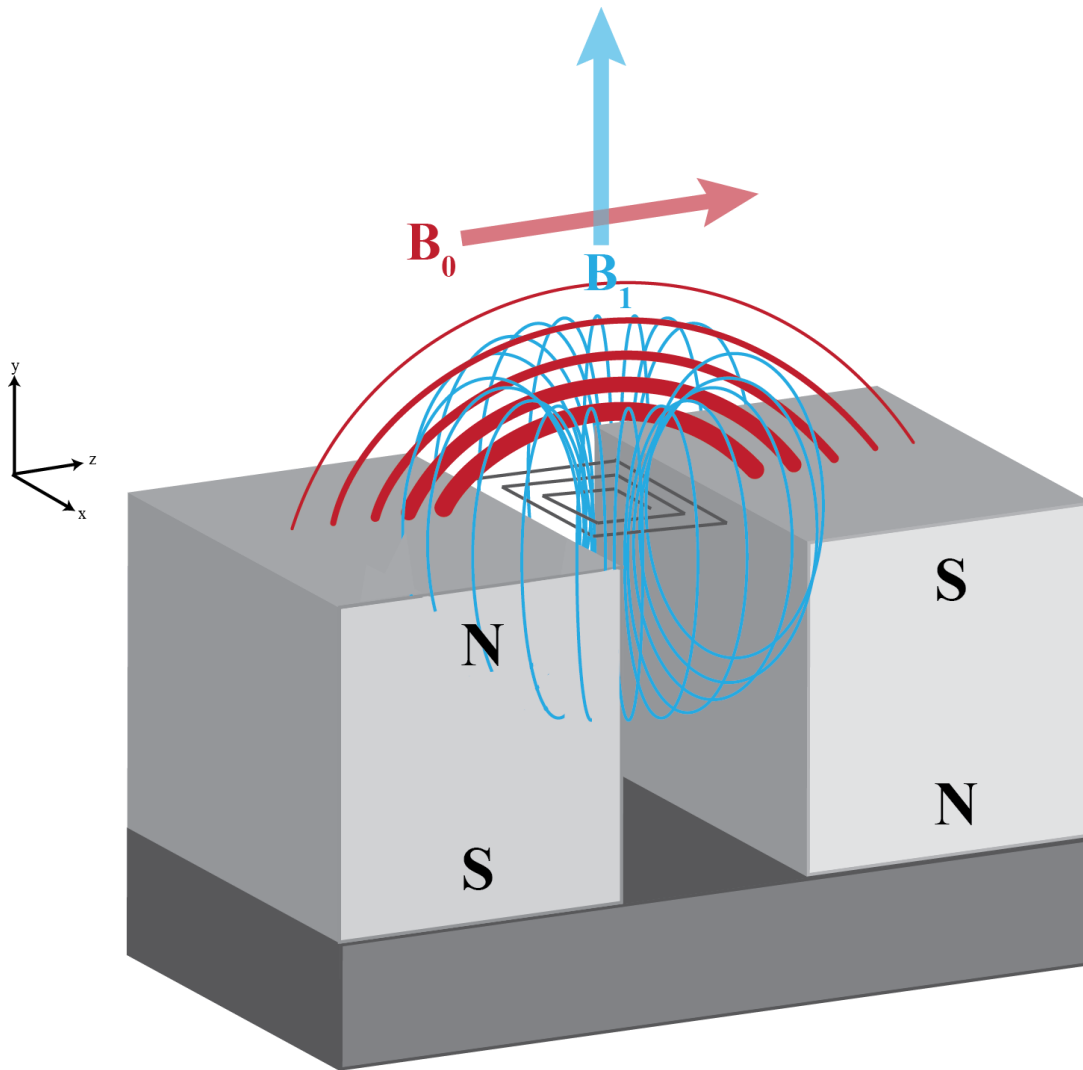


Figure 4: The NMR-MOUSE single-sided NMR apparatus, consisting of two permanent block magnets, which produce the inhomogeneous field B_0 (red). The intensity of B_0 decreases as a function of distance from the surface of the block magnets, as shown by the arcs of varying thickness. Positioned between the two block magnets is a radiofrequency coil (black) which produces the rf magnetic field B_1 (blue).

Both the B_0 and B_1 fields produced by the NMR-MOUSE are inhomogeneous, imparting a strong magnetic field gradient to the sensitive region of the instrument; the frequency of the B_1 field determines the magnitude of the gradient. [46] Therefore, nuclei at different distances from the surface of the magnets and coil experience varying field strengths. This makes it impractical to use single-sided NMR to gain information like chemical shifts, since these are only useful if it is assumed that all protons in like environments precess at the same frequency. By **Equation 2.1**, however, the frequency of precession is proportional to the magnitude of B_0 that a proton experiences, so even protons in like environments will precess at different frequencies depending on their location in a sample and their distance from the magnet's surface.

The sample data that single-sided NMR instrumentation can easily acquire are T_1 and T_2 relaxation times, which can be used to determine some of the physical properties of a material. Measurement of diffusion coefficients, which describe the motion of molecules in a sample, can also be performed since this sort of experiment is simplified by the magnetic field gradient inherent in single-sided NMR instrumentation.

T_1 relaxation, also called longitudinal or spin-lattice relaxation, occurs as the component of a sample's bulk magnetization vector parallel to B_0 returns to its equilibrium magnitude after perturbation with an rf pulse. The longitudinal relaxation time constant, T_1 , is determined from an exponential fit of the buildup magnetization in the z-direction after either an inversion or saturation-recovery pulse sequence is applied to a sample. [47] The resulting T_1 value can be used to study segmental motion in polymers since T_1 relaxation is related to fluctuations in the small transverse magnetization created by the changing dipoles of rotating molecules. [43] T_1 values are

heavily temperature and field dependent, which makes them less practical measurements for gathering concrete information about a sample. They are useful, though, for determining the amount of time to wait between successive $\pi/2$ excitation pulses in a Carr-Purcell-Meiboom Gill (CPMG) experiment, discussed later, which is used to measure T_2 relaxation times. Since T_1 values are measured by timing the recovery of magnetization in the z-direction after a pulse is applied, they give the minimum amount of time that spins in a sample need to recover equilibrium after perturbation, and therefore the minimum amount of time to wait before beginning a new pulse sequence iteration. The repetition time for a CPMG experiment is usually set to five times the T_1 value of the sample of interest. This study, though, does not include measurement of T_1 values or diffusion coefficients, and concerns itself solely with examining transverse relaxation times.

Transverse relaxation, also called spin-spin relaxation, occurs as the component of a sample's net magnetic moment perpendicular to an applied magnetic field decays. This decay is caused by the gradual decoherence of the precessing spins of the individual excited nuclei in the sample, which are precessing at different frequencies in an inhomogeneous field, as noted above. Since all the spins are precessing differently, their precessional motion loses synchrony and the spins dephase. At this point, the spins' magnetization vectors are distributed randomly and there is no longer an observable net magnetization in the xy plane and the FID signal dies out. [43, 48] The transverse relaxation time constant, T_2 , characterizes the time necessary for the precessing spins to lose coherence. Samples with highly rigid molecular structures display small T_2 values, since isotropic motion within the sample is limited, increasing the dipolar interactions

between spins and hastening the dephasing of these spins. Larger T_2 values are typical of samples that allow free molecular motion, since dipolar interactions average out as different nuclei interact, preserving spin coherence. In polymers, mobile chains indicate free molecular motion, and thus polymer networks with chains that are crosslinked or adsorbed onto a surface exhibit a smaller T_2 than bulk polymer samples. [49]

T_2 relaxation time however, cannot be measured by single-sided NMR using the same simple pulse-acquire experiment used in traditional NMR, like the one shown in **Figure 3**. Since the Larmor frequencies of protons in different parts of a sample in an inhomogeneous field are not equal, the protons' spin axes are tilted at a variety of angles after application of an rf pulse, rather than all at the same angle as they would be in a homogeneous B_0 . The majority of the spins, then, are out of phase even while the rf pulse is still being applied. Therefore, the total decoherence of the spins after the end of an rf pulse by a coil in a single sided-NMR occurs very quickly, usually in an amount of time similar to the "dead time" of the coil, during which signal cannot be acquired. This dead time is the length of time it takes for residual energy in the rf coil, left over from generating an excitation pulse, to dissipate. The rf coil in most NMR instrumentation is used both for applying an excitation pulse and for detecting the signal from the precessing nuclei after excitation, so if it were used for detection immediately following excitation with leftover energy still in it, it would record a phantom signal originating from that energy in addition to the signal from the precessing nuclei. If the signal attenuation time and dead time are similar in length, it becomes impossible to collect an FID.

Single-sided NMR instruments instead measure T_2 relaxation time using the Carr-Purcell-Meiboom Gill (CPMG) pulse sequence, during which a series of Hahn echoes are collected. [39] A Hahn echo is obtained by refocusing the dephased magnetization vectors of nuclei in an inhomogeneous field as they precess following excitation by an rf pulse. [50] This is done by applying an initial $\pi/2$ pulse to the sample and allowing the nuclei to precess and the resulting signal to decay as usual for a specific amount of time, τ , that is longer than the dead time of the rf coil. At the end of time τ , a second rf pulse, a π refocusing pulse, is applied. The π pulse reflects the bulk magnetization, and therefore each precessing spin, over the x- or y-axis, depending upon the axis to which the $\pi/2$ pulse first tilted the vector. By refocusing the precessing spins in this way, the chemical shift values of the nuclei are also refocused, making it impossible to collect these values using echoes.

After the π pulse ends, the spins' motion then resumes and each individual magnetic moment returns to the point where it started when the $\pi/2$ pulse was applied. This convergence of the spins to their origin produces an "echo" of their original FID signal, from which the amplitude of that original signal can be determined. The amount of time required for the spins to reconverge after the application of the refocusing pulse is exactly the same as the length of time between the two pulses, τ , so signal appears long after the dead time of the coil and the receiver can easily detect it. The amount of time that elapses between the onset of the $\pi/2$ pulse and the appearance of the Hahn echo, equal to 2τ , is called the "echo time". A vector representation of precession and refocusing during the generation of a Hahn echo is shown in **Figure 5**.

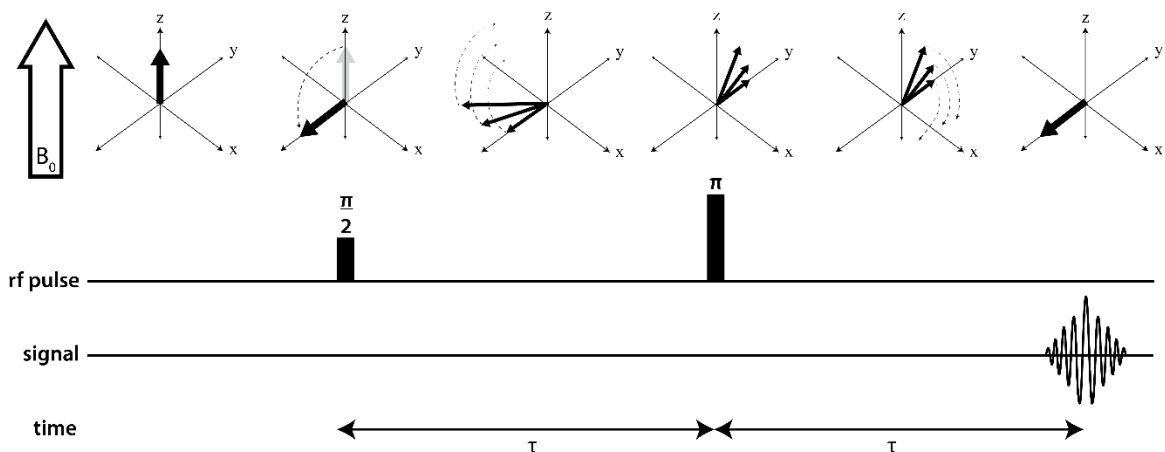


Figure 5: Diagram of a Hahn echo experiment in the same format as Figure 3. The first set of axes shows a sample that has equilibrated in an applied magnetic field, B_0 , and has developed net magnetization in the direction of B_0 . Next, the $\pi/2$ pulse is applied, moving the net magnetization vector into the xy-plane. After the pulse ends, the magnetization vectors of the individual nuclei precess around B_0 at different frequencies due to field inhomogeneities. This precession is permitted to continue for some time τ which is longer than the dead time of the NMR receiver coil. At this point, a π refocusing pulse is applied to flip the magnetization vectors over the x axis, reversing the direction of their precessional motion. The magnetization vectors continue precessing until they reconverge at their starting point at time τ after the π pulse, generating the Hahn echo.

In a CPMG pulse sequence, detailed in **Figure 6**, multiple π refocusing pulses are applied after the initial $\pi/2$ pulse, creating a chain of echoes that appear at regular intervals denoted by the echo time. Over time, the echoes themselves decrease in amplitude and die out as a result of spin decoherence. This echo decay train can therefore be used to determine the T_2 of a sample by graphing data points generated using the equation

$$\frac{S}{S_0} = e^{\frac{-t}{T_2}} \quad (2.6)$$

where S is the signal intensity of an echo, S_0 is the intensity of the echo with the highest observed amplitude, which is used to normalize the data points, t is the length of time after the excitation pulse, and T_2 is the transverse relaxation time constant. The natural log of the normalized signal intensity of each echo plotted with respect to time will form a line with the slope $-1/T_2$, making it simple to determine the T_2 value of a sample. In order to increase the signal-to-noise ratio of the acquired data, and therefore the precision of the measured T_2 value, fits of the average signal collected from repeated CPMG pulse sequences (separated by the repetition time discussed above) are often used.

The T_2 value determined using this fit of the echo train decay amplitudes is not actually the true T_2 of the material, which would be the measure of the spin decoherence within one echo. The fit of the echo train instead gives the value of the effective transverse relaxation, denoted $T_{2,\text{eff}}$, which is a mixture of T_1 and T_2 and is dependent on experimental parameters, particularly the echo time used. The $T_{2,\text{eff}}$ and T_2 values measured for a sample would be the same if $T_1/T_2=1$ or if the echo time of the experiment were set to zero. [47] For the sake of convenience, however, $T_{2,\text{eff}}$ and T_2 will be considered interchangeable in this paper and will be referred to only as T_2 .

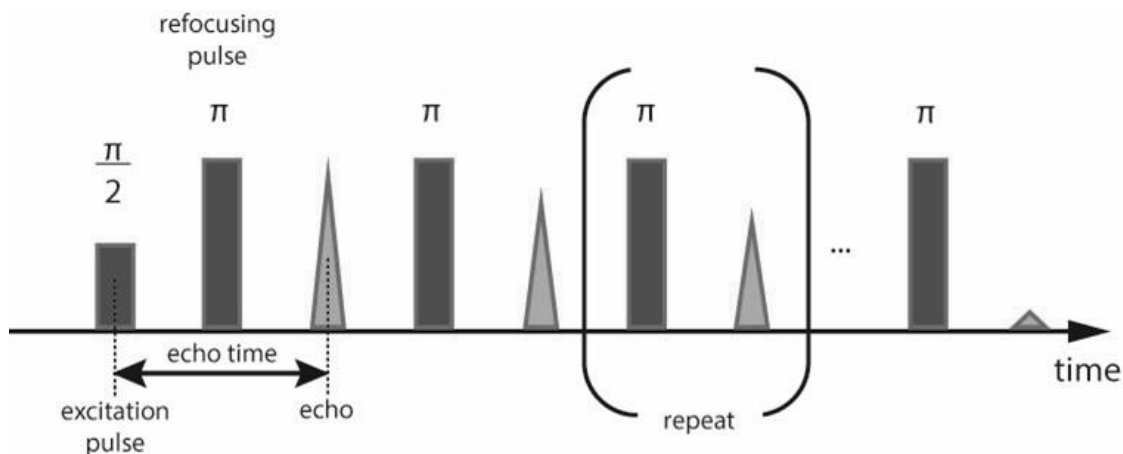


Figure 6: The CPMG pulse sequence. A $\pi/2$ excitation pulse and a π refocusing pulse are applied to a sample, after which a Hahn echo is collected (as shown in more detail in Figure 5). Once the first echo appears, another π pulse is applied after time τ in order to generate a second Hahn echo. The second echo has a lower amplitude than the first as a result of relaxation. The process of refocusing magnetization and collecting echoes is repeated until no more echoes appear. Each echo occurs after the same amount of elapsed time, referred to as the echo time. The echo train decay can then be modelled with an exponential function to determine the T_2 of the sample.

Chapter 3: Acrylic Emulsion Paints & Pigment Volume Concentration

Acrylic emulsion paints were developed in the years following WWII as manufacturers were looking for new ways to use the synthetic polymers that had been developed in response to rubber shortages during the war years. [51] One company, Rohm and Haas, realized that a strong potential market for their emulsion polymer formulation was in producing paints for the swathe of new houses that returning soldiers were having built for their families. In 1953, the company patented their formula for synthetic water-based acrylic paint. This acrylic emulsion or “latex” paint had many advantages over traditionally used solvent-based paint because of its durability, low odor, vivid non-fading and non-yellowing color, easy cleanup with soap and water, and low toxicity. Within twenty-five years, latex paint had eclipsed oil-based paints for use on home exteriors and interiors. [2, 3, 51] The same qualities that made these paints attractive for homeowners also appealed to artists, and the first artists’ acrylic emulsion paints were sold by Liquitex in 1956. Other companies soon developed their own formulations, and the use of these synthetic paints skyrocketed in the 1960s and 1970s. Currently, acrylic emulsion paints are the mostly commonly used synthetic artists’ paint, and works created whole or in part with either artists’ acrylic paint or other commercial acrylic paints (house paint, synthetic car enamel, etc.) account for a majority of the objects in the collections of modern art museums worldwide. [3]

To manufacture acrylic emulsion polymers, acrylic monomers are synthesized and then introduced into an aqueous solution with the help of a non-ionic surfactant, often a sulfonate or a fatty acid. [2, 52] The most commonly used monomers for acrylic emulsion paint are methyl methacrylate (MMA) and n-butyl acrylate (nBA), shown in **Figure 7**.

Early acrylic paints used a copolymer of MMA and ethyl acrylate (EA); however, EA was replaced by nBA, which creates films that are more durable and hydrophobic. [3]

When the solution is agitated, the surfactant coalesces into micelles with a few hydrophobic monomers on the inside; other monomers are left undissolved outside the micelles and congregate in large monomer “droplets”. A small amount of a radical initiator such as a peroxide is then added. The initiator fragments diffuse into the monomer-filled micelles, usually only one per micelle, since the concentration of initiator is low, and begin polymerizing the monomers within, forming a “polymer particle”. As the polymerization reaction progresses and the monomers inside the particle are used up, more monomers from the undissolved droplets outside diffuse in to continue the process. Each particle grows to approximately the same molecular weight since each original micelle contains one initiator and a similar number of monomers. The reaction terminates when another radical diffuses into the particle. Since there are only a few initiator fragments in solution, it takes a long time for the reaction to terminate and the resulting particles have a very high molecular weight. [53]

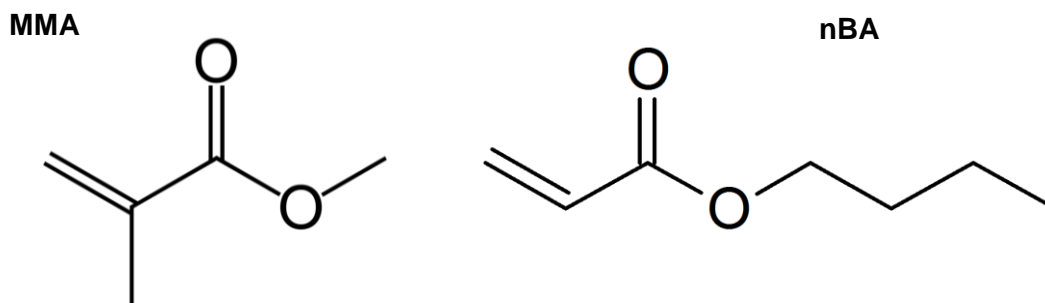


Figure 7: Methyl methacrylate (MMA) monomer (left) and n-butyl acrylate (nBA) monomer (right), which are used in the radical-catalyzed polymerization of acrylic emulsion polymers for use in acrylic emulsion paints.

To modify the polymer dispersion for sale as a paint, various stabilizers, fillers, and other materials need to be added to ensure optimal performance. [1–4] Buffers are needed to prevent the paint from developing a low pH which could compromise the integrity of a painting. Fillers like glass particles are added to increase the body of the paint and make it easier to manipulate. Defoamer is included to prevent air bubbles from forming in films. Biocides are added to prevent mold and mildew formation in the wet paint or on the dry films. Most importantly, pigments, and pigment dispersal agents, are added to give the paint color.

A quantitative measure of the level of pigmentation in a paint is the pigment volume concentration value (PVC). [54] The PVC of a paint film has also been shown to have a significant effect on many of the film's other physical characteristics such as glass transition temperature, water permeability, aging processes, tensile strength, and elastic modulus. [19, 54-57] It can be calculated using the following equation:

$$PVC = \frac{V_p}{V_b + V_p} \quad (3.1)$$

where V_p is the volume of the pigment, calculated using the mass of pigment used and the pigment density, and V_b is the volume of the nonvolatile portion of the base.

As the PVC of a paint film increases, a point is reached at which the amount of binder is just enough to coat the pigment particles with a thin shell composed entirely of adsorbed binder and fill the voids between them. This point is referred to as the critical

pigment volume concentration [56], and can be calculated using the formula

$$CPVC = \frac{I}{I+(OA)(\rho_p/\rho_b)} \quad (3.2)$$

where OA is the pigment oil absorption, which is listed on the pigment manufacturer's website or in artists' handbooks, ρ_p is the density of the pigment, and ρ_b is the density of the nonvolatile portion of the binder.

As the pigment concentration in a paint film approaches the CPVC, a clear change can be observed in many of the physical and mechanical properties of that film. These changes include a decrease in gloss, elastic modulus, blistering, and scrub resistance and an increase in permeability, opacity, rusting, and porosity as a result of the lack of binder and incorporation of air voids into the film. [56, 58-60]

To facilitate comparison of the changes in paint film properties as a function of increasing pigment concentration while keeping in mind the varying CPVCs of different binder/pigment systems, the reduced pigment volume concentration (Λ) is used as:

$$\Lambda = \frac{PVC}{CPVC} \quad (3.3)$$

This parameter allows one to look at films made with different pigments or different binders at identical particle packing levels, and helps determine which property changes can be viewed as dependent on pigment type. [61] A simplified representation of the binder/pigment interactions at different Λ values is given in **Figure 8**.

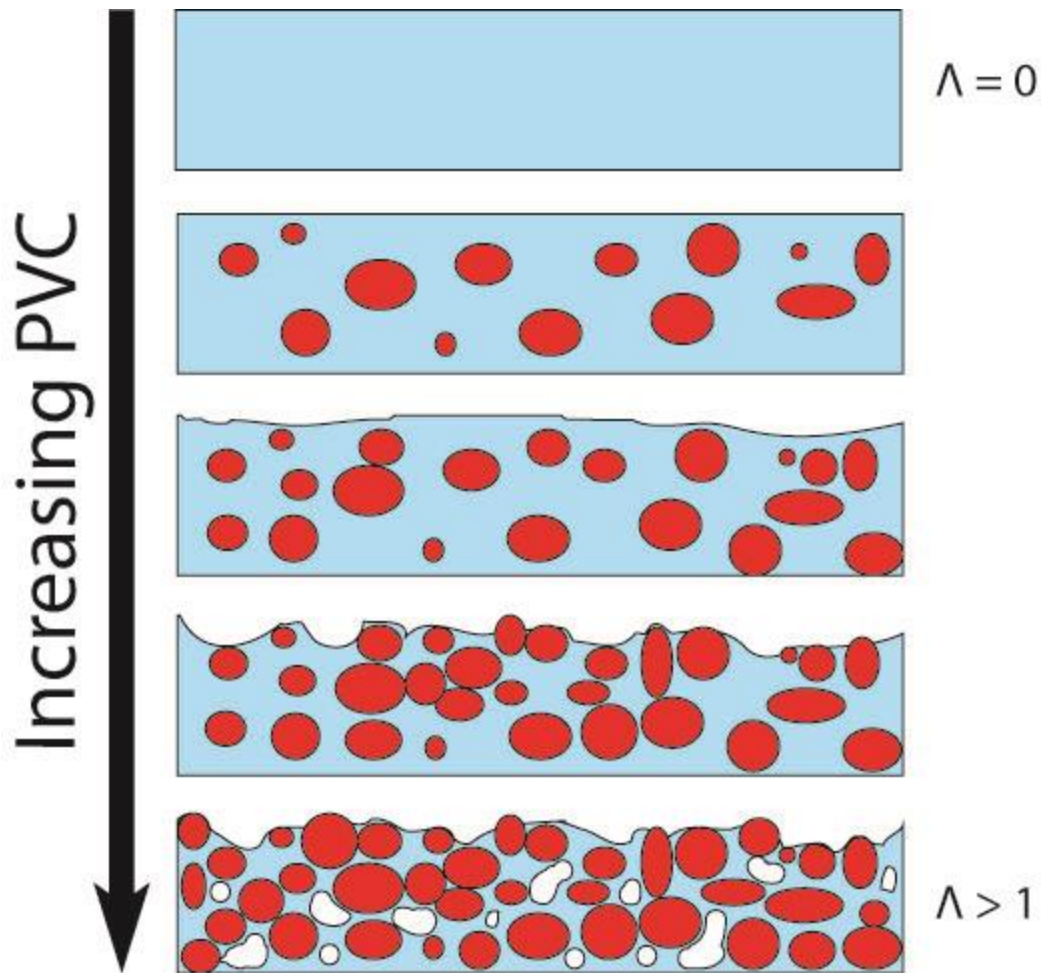


Figure 8: The changes in a paint film as Λ is increased. At the top is an unpigmented film, $\Lambda=0$, made up of pure acrylic binder. As pigment is added and Λ increases, the film becomes disrupted as more binder is adsorbed to the surface of the pigment particles. Above the CPVC, when $\Lambda>1$, air voids begin to form in the paint film and all binder is adsorbed to the pigment particles. Figure adapted from [62].

Since artists use not only paint produced specifically for art applications, but also acrylic paint meant for houses, cars, and other industrial applications, a variety of different pigments in different concentrations appear in artwork. Paints for different purposes are often formulated with different amounts of pigment, depending on the desired paint characteristics. Interior house paint is often formulated with more pigment than binder, which gives it more of a matte appearance, greater opacity, and better coverage. Exterior paints have a higher binder to pigment ratio, which increases their water resistance and durability. Even artists' paints have varying pigmentation levels depending on the desired properties, the color, and the relative cost of the paint (cheaper paints have less pigment). [3] As previously mentioned, the level of pigmentation in a paint film has a significant influence on the film's physical properties. Therefore, a comprehensive study of the properties of acrylic paints with different PVCs is essential to better understanding acrylics and leading to better-informed conservation practices.

The rate at which a paint film cures is another property influenced by its pigment volume concentration. Studies using transmission electron microscopy (TEM) and atomic force microscopy (AFM) have shown that acrylics cure in a three step process with four distinct stages (shown in **Figure 9**) that can be finished within a matter of weeks or even days, depending on the film thickness. [63-68] This quick drying time is one of the most attractive qualities of acrylic paint, both for artists' and house paints.

The first step in this process is evaporation of the volatile component of the acrylic emulsion. This causes a transition in the paint binder from acrylic particles suspended in an aqueous solution to individual particles deposited on a substrate with a small amount of water retained in the voids between particles. These particles then

deform as solvent evaporation completes, creating a densely packed array of particles with no spaces in between, but which still retain their individuality. Finally, polymer chains diffuse between adjacent particles, resulting in formation of a continuous film. [64, 65, 67-71] This film is quite durable and cannot be redissolved with water.

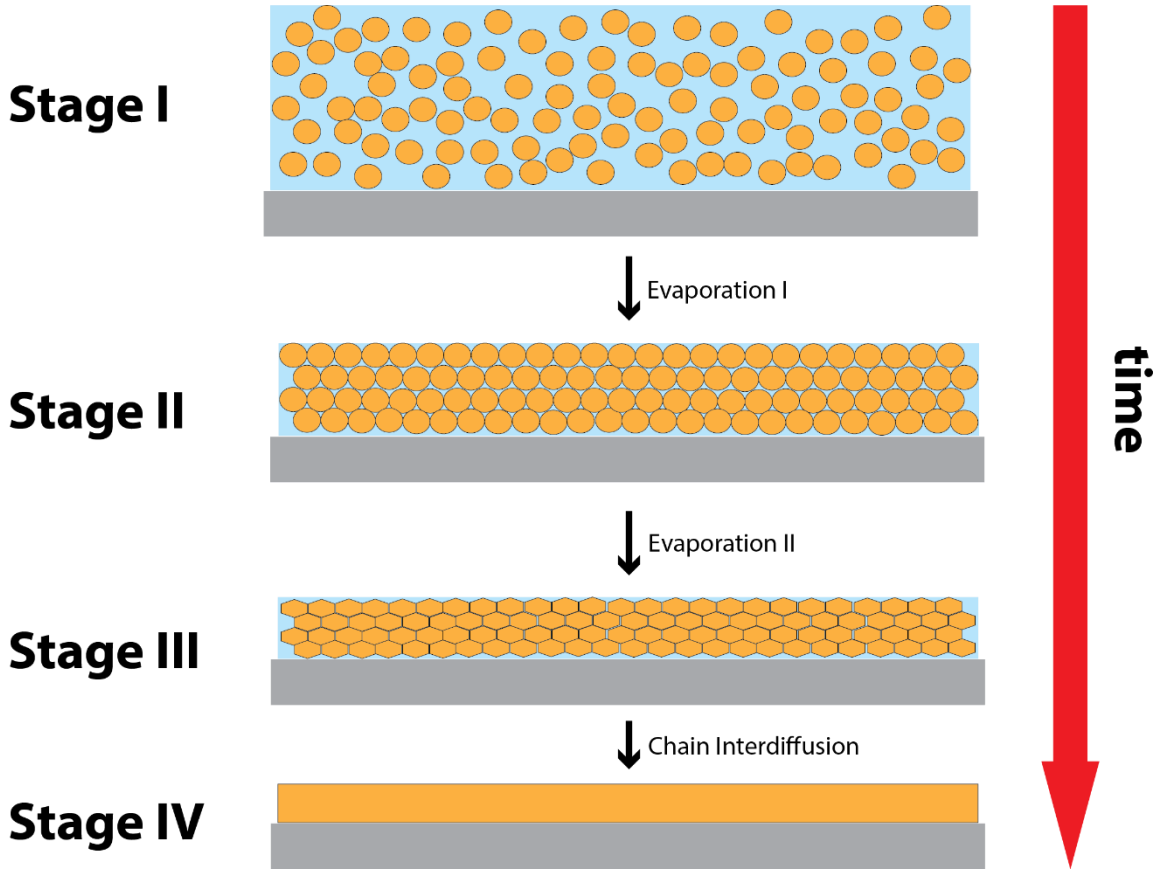


Figure 9: The stages in the acrylic curing process. Stage I shows acrylic particles suspended in an aqueous solution, which begins to evaporate and push the particles closer together resulting in Stage II, where the particles are densely packed but still have voids containing solution between them. The solution in the voids later evaporates and causes the particles to deform, as shown in Stage III. Polymer chains then begin to diffuse between the deformed particles, and the particles lose their individuality and form a continuous film. Figure adapted from [63].

Since the acrylic curing process requires no more than a few days for samples less than a millimeter thick [70,71], the paints prepared in the current study, which were allowed to age under ambient conditions in a temperature and humidity controlled laboratory for a minimum of four weeks before measurements were taken, are presumed to be uniformly cured. Differences in film curing, then, cannot account for different film T_2 values (discussed in Chapter 2), which are often considered characteristic of areas of more or less crosslinking or curing extent when studying oil paints using NMR. Unlike acrylics, oil paints form a cured film in a two-step process: the volatile compounds in the wet paint evaporate, and then the fatty acids which make up the binder begin to crosslink in an autoxidative process that can take years to complete fully. [49] Parts of the paint films that are closer to the surface, and therefore closer to air and more easily oxidized, exhibit smaller T_2 values than less cured regions in the films' interiors. This interpretation should not work when looking at the acrylic paint films in this study, however, since acrylic paints cure far more quickly than oils and in a manner that is not reliant on oxygen diffusion into the paint layers. However, in polymers, mobile chains indicate free molecular motion, and thus polymer networks with chains that are adsorbed onto a surface (such as a pigment particle) exhibit a smaller T_2 than bulk polymer samples like binder that is not interacting with a surface, which will be discussed in Chapter 5. [72]

Chapter 4: Materials & Methods

Paint Sample Preparation:

Acrylic emulsion paint samples were prepared in varying concentrations for four commonly used pigments, two organic (phthalo blue, color index PB 15:3, product #23060, and alizarin crimson, color index PR83, product #23610) and two inorganic (ivory black, color index PBk 9, product #47200, and titanium white, color index PW6, product #46200), purchased from Kremer Pigmente (New York, NY). Titanium white pigment has a chemical formula of TiO_2 and ivory black is a mixture of CaCO_3 , $\text{Ca}_5(\text{PO}_4)_3(\text{OH})$, and amorphous carbon. The structures of the organic pigments used are shown in **Figure 10**.

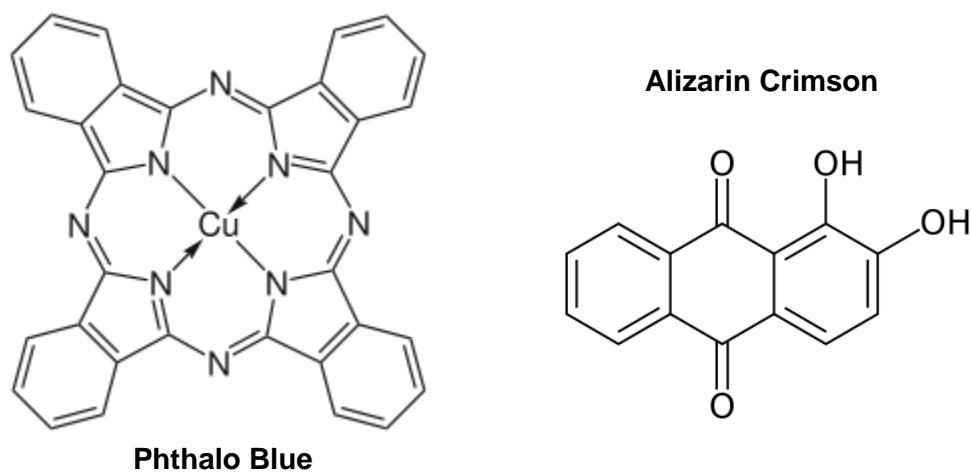


Figure 10: Structures of phthalo blue (left) and alizarin crimson (right).

Ivory black and titanium white samples were produced by weighing out dry powdered pigment and wetting it with deionized water. The water/pigment mixture was ground on a glass slab using palette knives until it reached a gel-like consistency, at which point a previously-weighed portion of either Golden Semi-Gloss Regular Gel Medium (Golden Artist Colors, Inc., New Berlin, NY, item #3040) or Regular Gel Medium (Golden Artist Colors, Inc., New Berlin, NY, item #3020) was added. Mixing continued until the pigment appeared evenly distributed in the base. Samples of the prepared paints were drawn down with a drawbar (Elcometer, Rochester Hills, MI) set to 200 μm on 1" by 3" glass microscope slides; this resulted in dry films approximately 50 μm thick. A minimum of three slides were made for each pigment concentration. Photographs of the paint making process and finished slides are included as **Figures 11** and **12**, respectively.

Phthalo blue and alizarin crimson samples were made in a nearly identical manner, except that ethanol (ACS grade, 200-proof, Pharmco-AAPER, Brookfield, CT) was used for initial wetting of these organic pigments instead of deionized water. Once the dry pigment was thoroughly coated in ethanol, deionized water was added and the pigment mixture was ground to a gel like-consistency as before. If ethanol alone was used, the paint sample became too dry and sticky to allow the deposition of a smooth film on the glass slides.



Figure 11: Paint being made in a fume hood. Ivory black pigment and deionized water are ground together with palette knives on a glass slab until they reach approximately the consistency of toothpaste. Afterwards, acrylic base is added and mixing continues in the same manner until pigment is evenly distributed in the binder.

Films of plain acrylic base with the same thickness as the pigmented samples were also prepared for comparison, using both the Semi-Gloss Regular Gel Medium and the Regular Gel Medium used in preparing the paint samples.

The PVC of each paint sample was calculated using **Equation 3.1**. The nonvolatile percentage of the acrylic base had been previously determined by measuring the decrease in mass of five samples of base as they dried over a period of two weeks (or

until no change in mass was detected). Volumes were calculated using the pigment densities (available on the Kremer Pigmente website) and the density of the dried acrylic binder, which was measured experimentally by observing the change in volume when a preweighed dry binder film was placed in a graduated cylinder of deionized water.

CPVCs for each of the pigments were calculated with **Equation 3.2**. The oil absorption values for each pigment were taken from the Kremer Pigmente website, or if that information was not available there (as in the case of phthalo blue and alizarin crimson) these values were taken from the Artist's Handbook. [73] Pigment and binder densities were determined as described above.

Once both the PVCs and CPVCs had been calculated, Λ values were calculated for all pigment/binder combinations using **Equation 3.3**. The CPVCs of each pigment can be found in **Table 1**, and the PVCs and Λ values for all paint samples can be found in **Table 2**, both in **Appendix A**.

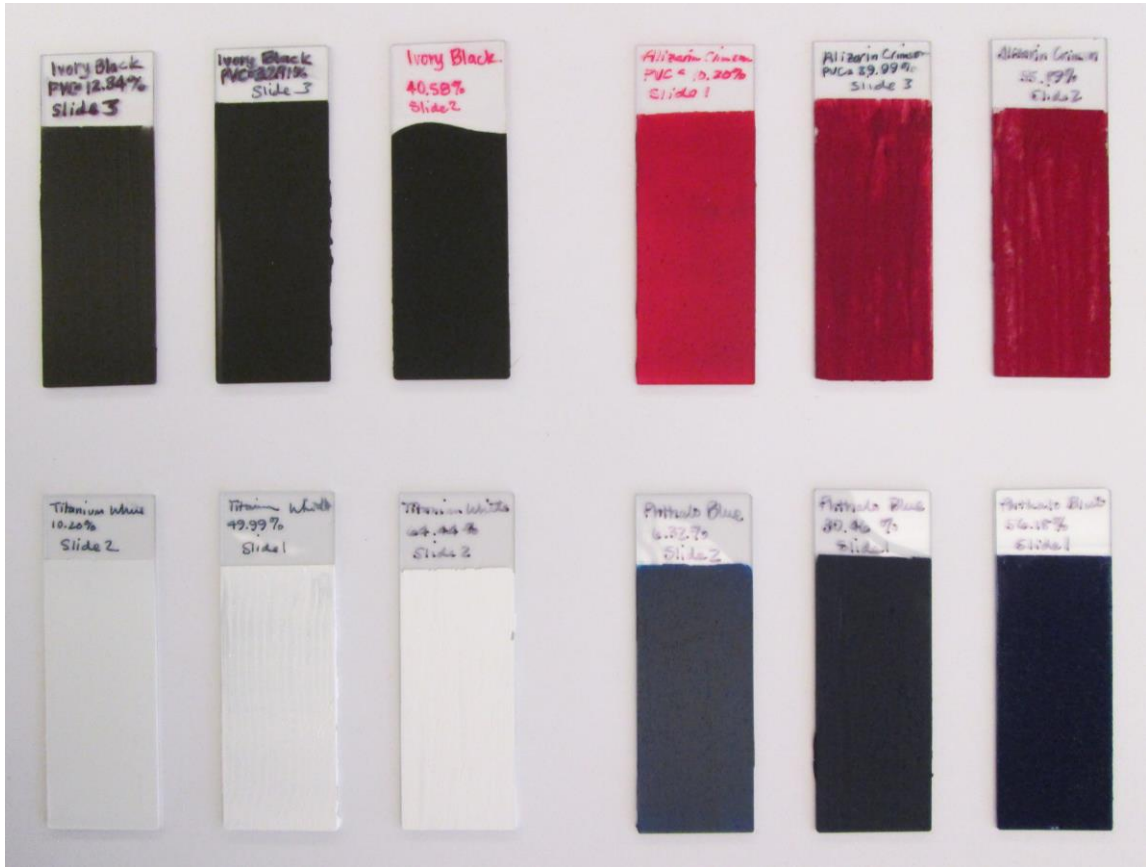


Figure 12: A selection of cured paint samples made with each of the four pigments (clockwise from top left: ivory black, alizarin crimson, phthalocyanine blue, and titanium white) at various pigment volume concentrations. Paint film PVC increases from left to right across each sample group. Note the visible difference in color and texture as PVC increases, especially evident in the alizarin samples.

Gloss Measurements

Gloss measurements were taken using an ETB-0686 Glossmeter (M&A Instruments Inc., Arcadia, CA) with a beam angle of 60° and a range of 0-200 gloss units (GU). This instrument determines the relative gloss of a sample by shining a beam of light at a sample at a certain angle and recording the amount of light that reflects back from it. This amount of light is compared to the amount of light that reflects from a piece of black glass used as a standard. The ratio of these two quantities is flashed on a digital display in the arbitrary unit GU. The gloss of each paint sample was determined as the average of measurements at three separate points on each of the three slides for each unique pigment/concentration combination.

Single-Sided NMR

NMR analysis was performed using a PM 5 NMR-MOUSE single-sided NMR (Magritek, New Zealand) with a field strength of approximately 0.4 T (19.27 MHz proton frequency) and a field gradient of 23.5 T/m connected to a Kea2 spectrometer (Magritek), shown in **Figure 13**, after the samples were allowed to dry a minimum of four weeks. The PM 5 NMR-MOUSE coil can take measurements of a 25 mm by 25 mm sample area, and can obtain signal from a depth of a maximum of 5 mm into a sample. The maximum depth can be altered by adding up to two 2 mm spacers to the magnet; adding spacers reduces the maximum depth but increases the amount of signal that be detected during a measurement while also shortening the minimum echo time and pulse length that can be used. All measurements performed for this study were done with both spacers in the instrument since the T_2 values of the acrylic films were very short and required a

short echo time to observe, and because the samples were very thin and produced very faint signal if placed too far from the rf coil. The magnet's vertical distance from a sample can also be adjusted in increments of 10 μm with a lift (Magritek) in order to find the area with the greatest signal intensity. The magnet, spectrometer, and lift are all controlled by a laptop running the program Prospa (Magritek), which also records the signal generated during experiments.



Figure 13: The NMR-MOUSE apparatus used in our lab. The PM5 magnet itself (black, with blue stripe) is housed in the lift (aluminum frame). To the left, the Kea2 spectrometer is visible. An ivory black paint sample sits in the sensitive region atop the magnet.

Before the T_2 of an acrylic sample was collected, a profile experiment, in which CPMG measurements are performed at incremental depths, was run to determine the region of greatest signal intensity within the sample. All samples were shown by the NMR measurements to be about 50 μm thick, and the lift height was adjusted so that CPMGs could be run at approximately the middle of the sample. Sample profile data is given in **Figure 14**, and profile parameters can be found in **Appendix B**. Within **Figure 14**, the left-hand plot shows the echo decay collected during the last CPMG experiment in the profile (which shows only noise here; a curve with an exponential decay would be visible if signal were detected), and the right-hand plot shows the amplitudes of the signal acquired at each depth. Each line on the profile plot (right) is generated by adding different parts of the echo decay train to get signal intensity with different T_2 weighting. If only the first few echoes in the decay are used, the signal intensity observed is dependent only on the proton density of the sample, whereas using the full echo decay gives a signal intensity based on both the proton density and T_2 of the sample. Because of the signal phasing used in the current experimental parameters, the area of greatest signal intensity corresponds to the minimum amplitude observed on the profile plot.

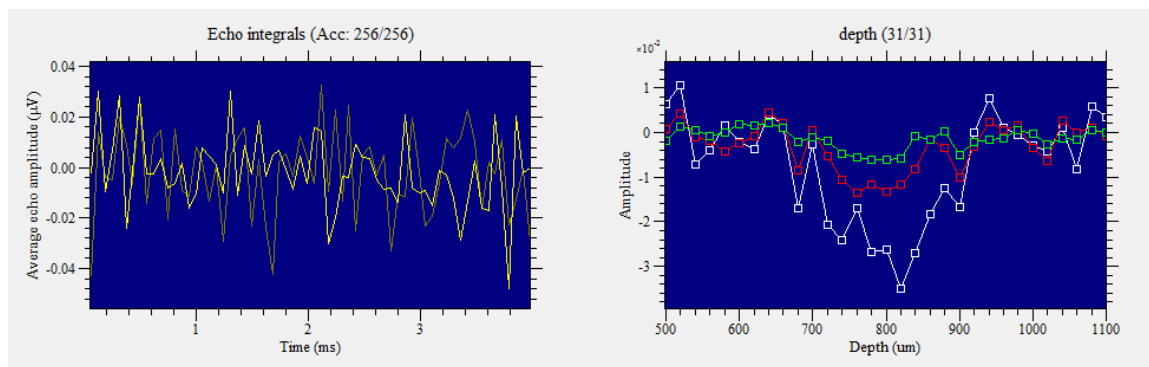


Figure 14: Results of a profile experiment for an alizarin crimson paint sample with $\Lambda=0.15$, generated using the Prospa software. The area of greatest signal intensity corresponds to the minimum amplitude observed at a depth of around 820 μm . The areas of low signal intensity above and the peak in the middle correspond to the air above the sample and the glass slide on which the paint sample is mounted, neither of which produce signal. The magnet was therefore moved to the 820 μm position before CPMG experiments were performed.

Each sample is slightly different, however, so the first of the three CPMG experiments performed on each sample was processed using a Fourier transform to ensure that the measurement was actually localized at the point of greatest signal. Adjustments of up to 100 μm in either the positive or negative z direction were occasionally necessary; if an adjustment was made in the sample height, three new CPMGs were performed and the original one was discarded. The same Fourier transform output was also used to approximate the thickness of the sample, as shown in **Figure 15**. The determination of spatial information through a Fourier transform of the single-sided NMR data is made possible because the transform analyzes data from the frequency domain. Since the B_0 field of a single-sided NMR has a gradient, protons at different distances from the magnet are precessing at different frequencies, and all protons at a given depth will precess at the same frequency, encoding spatial information in the

frequency data. For example, since B_0 is stronger closer to the magnet, by **Equation 2.1** protons closer to the magnet will precess at a higher frequency than those farther away. Depths where no signal is recovered correspond to empty space above and non-proton containing material (glass slide) below the sample. Performing a Fourier transform on the signal produced by the precessing nuclei in the inhomogeneous field separates the different frequencies making up the detected signal, and can therefore discern the depths of the nuclei in a sample, as well as the thickness of the sample, provided that the sample does not extend outside the magnet's sensitive region.

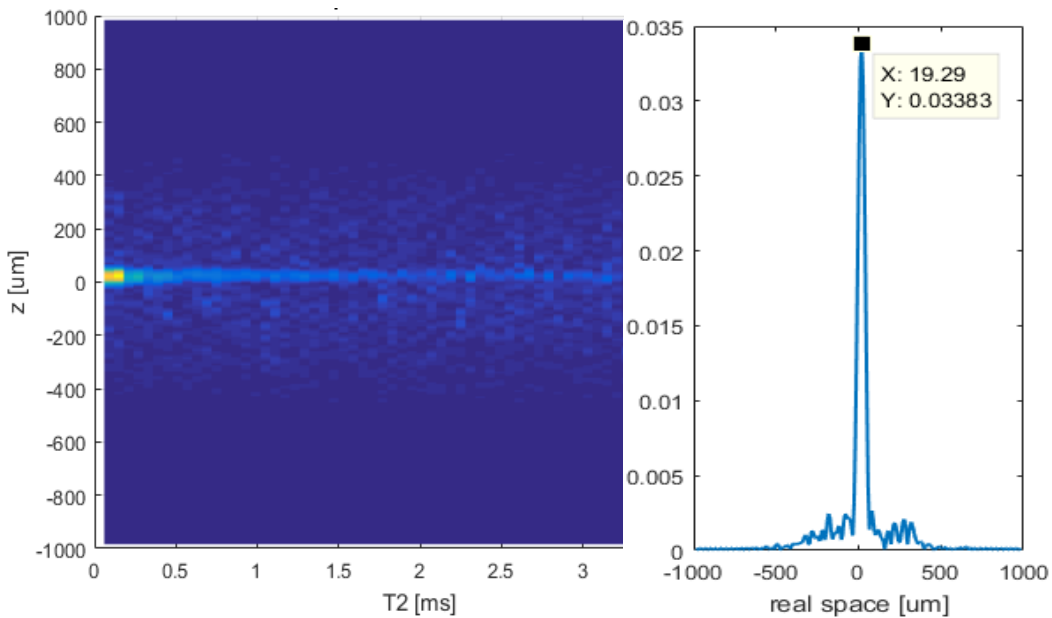


Figure 15: Fourier Transform of the echo train decay of an ivory black $\Lambda=0.15$ paint sample, generated using a MATLAB script and used to position samples at a level with maximum signal intensity. On the right, one can see that signal is obtained over an area of approximately $50 \mu\text{m}$, corresponding to the sample thickness, and the area of greatest signal intensity (yellow) is slightly above where the sensitive region of the magnet is positioned, at the $0 \mu\text{m}$ mark. The plot on the right is a “slice” of the plot on the left, with space on the x-axis and signal intensity on the y-axis. This makes it easier to determine the signal maximum, which in the case of this sample is $19.29 \mu\text{m}$ above the magnet's sensitive region.

For T_2 collection, three CPMG experiments with a pulse length of 2.75 μs for both the π and $\pi/2$ pulses, pulse amplitudes of -4 for the π pulse and -10 for the $\pi/2$ pulse, and an echo time of 60 μs , during which 64 echoes were collected, were performed on each paint slide at the position determined during the profile measurements. Each T_2 measurement comprised 2048 acquisition scans for a total measurement time of 17 min. The sets of three CPMG experiments for each sample were programmed to run one immediately following the other by a script developed in our lab and run through Prospa's debugger, into which all experimental parameters can be entered. The Prospa script and the CPMG parameters can be found in **Appendix B**.

Scanning Electron Microscopy/Energy Dispersive Spectrometry (SEM-EDS)

The air-contacting surface of the paint films was imaged using a Phenom Pro-X scanning electron microscope (PhenomWorld) in order to examine the distribution and size of the pigment particles in the film. Samples were excised from the microscope slide films using a razor blade, and images were collected using a beam intensity of 10 keV.

To determine the elements in the paint films, EDS analysis was carried out using the Phenom Pro-X's Element Identification (EID) software package on the areas of the paint films imaged with the SEM. Atomic concentration percentages and maps of the element concentration were collected with a beam intensity of 10 keV. The map resolution was 64 pixels, with a pixel time of 200 μs . Each map took approximately 45 minutes to acquire.

Data Processing

Single-sided NMR data was processed using MATLAB scripts (MathWorks Inc.; Natick, MA) developed in house. For each pigment/PVC combination, the full echo train decays for nine separate measurements were superimposed and analyzed with an Inverse Laplace Transformations (ILTs) in order to determine the number of unique T_2 values displayed by each sample. Since ILTs are by nature unstable and occasionally return ambiguous solutions, [74, 75] the full echo train decays for each data set were fit to either a monoexponential decay curve of the form

$$S(t) = Ae^{-t/T_2}$$

where t is the time in milliseconds and A is the signal intensity, or to a biexponential decay curve of the form

$$S(t) = Ae^{-t/T_{21}} + Be^{-t/T_{22}}$$

where t is again the time in milliseconds, T_{21} and T_{22} are the two unique T_2 values observed in the sample, and A and B are the signal intensities corresponding to each T_2 value. For initial exponential fits of data, where all data sets were processed with a monoexponential decay, the first two echoes of all CPMG echo train decays were omitted to reduce noise and account for inhomogeneities in the refocusing pulse. These exponential decays were fit using non-linear fitting parameters. The biexponential fit proved to model the echo decays more accurately than the monoexponential fit in low

PVC samples, confirming the presence of two unique T_2 values in paint films with pigment concentrations up to the CPVC. The R^2 values for the exponential fits were generally 0.85 or higher, and if the R^2 values for the monoexponential and biexponential fits were within 0.05 of each other, residuals calculated for the fits in the MATLAB curve fitting toolbox were used as the deciding factor in determining which fit was more appropriate. A comparison of a mono- and biexponential fit (with residuals) for the same paint sample is given in **Figure 16**, and numerical results for the exponential T_2 fits are given in **Appendix A, Table 4**.

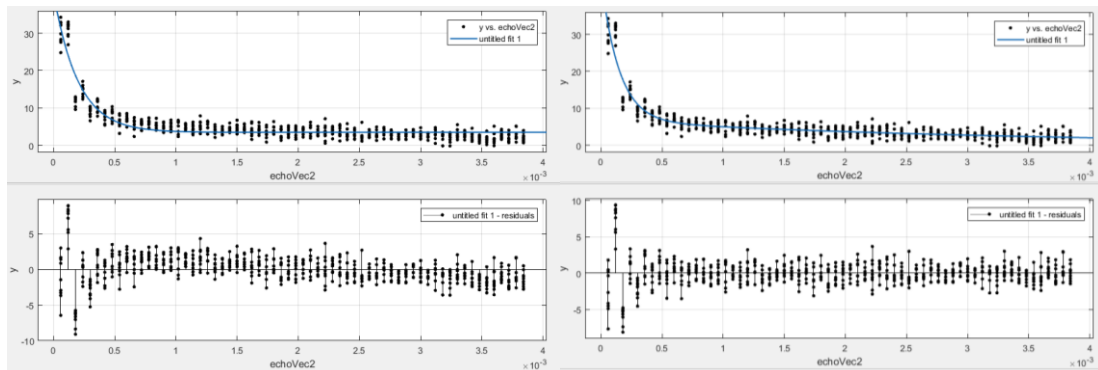


Figure 16: A monoexponential (top left) and biexponential fit (top right) of nine separate echo train decays measured for ivory black paint with $\Lambda=0.15$. The residuals for each, shown below their respective fits, mark the biexponential as more accurate since its residuals are distributed evenly around zero. The residuals for the monoexponential fit, on the other hand, shown an almost sinusoidal distribution around zero.

Chapter 5: Results and Discussion

When the PVC of a paint film increases, the surface of the film becomes disrupted. In low PVC films, pigment particles are uniformly submerged in the polymer, resulting in a smooth surface that easily reflects light. As the paint approaches the CPVC and the ratio of pigment to binder decreases, pigment particles clump together and begin to protrude from the smooth, glossy polymer matrix as is evident in the SEM images in **Figure 17**. The uneven surface creates more opportunity for incident light to scatter and therefore causes the gloss of the film to decrease. [61, 62, 76]

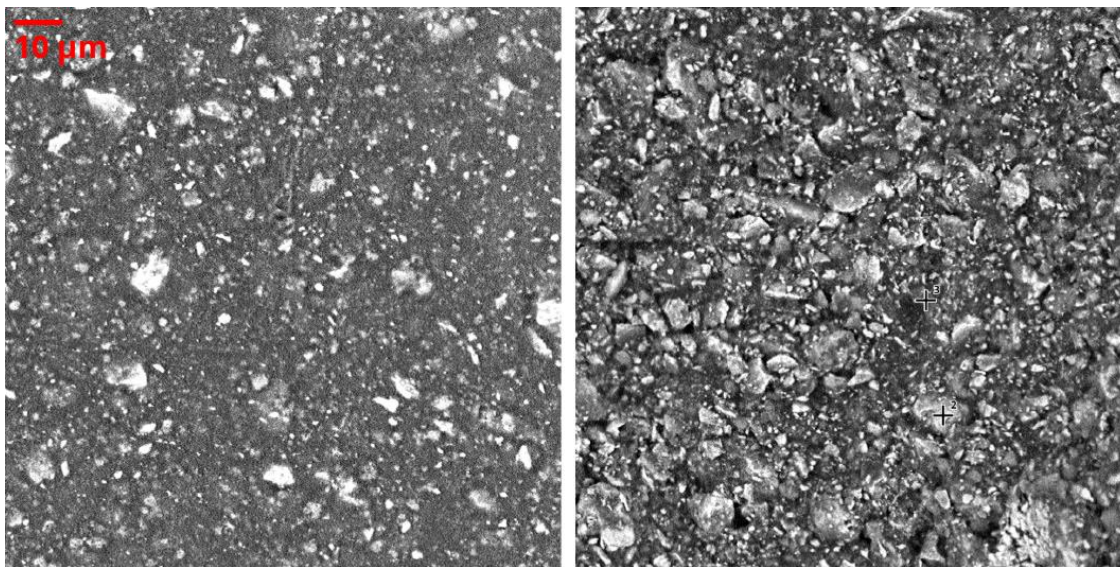


Figure 17: SEM images of ivory black paint formulated at pigment concentrations below (left, $\Lambda = 0.3$) and above (right, $\Lambda = 1.12$) the CPVC, showing decrease of binder and increased surface roughness, as well as pigment agglomeration.

The decrease in gloss observed for the paint films created in this study, shown in **Figure 18**, follows a curve similar to those published in the literature [62], given in **Figure 19**, confirming that paint films were correctly formulated.

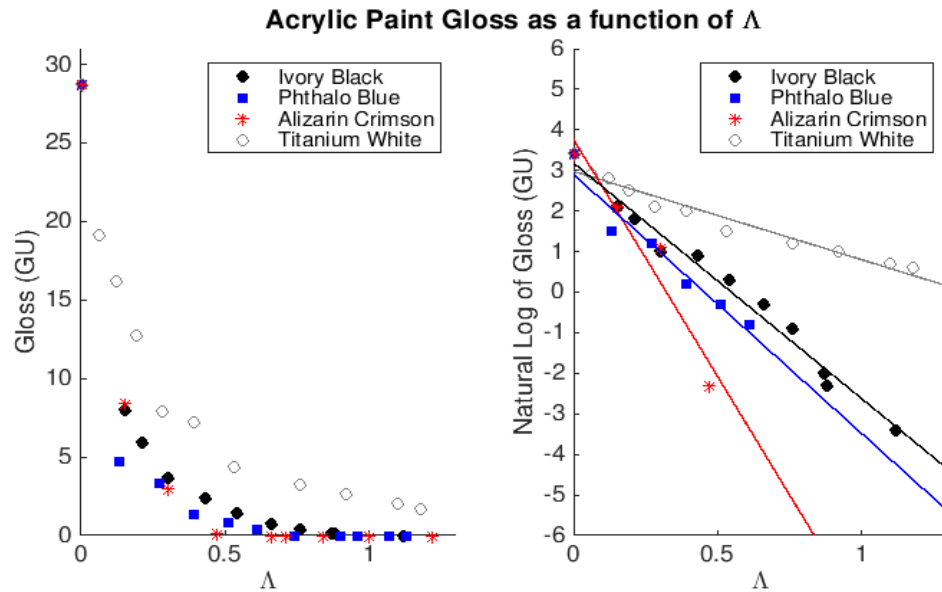


Figure 18: The change in gloss as Λ increases. Both the raw data and the natural log of the data have been presented, as the natural log better displays the trend in gloss, but the gloss values for certain pigments, such as alizarin crimson, decrease to zero too quickly to include all the points in the log plot. This was due to a lack of sensitivity in the instrument in measuring the reflectance of matte surfaces.

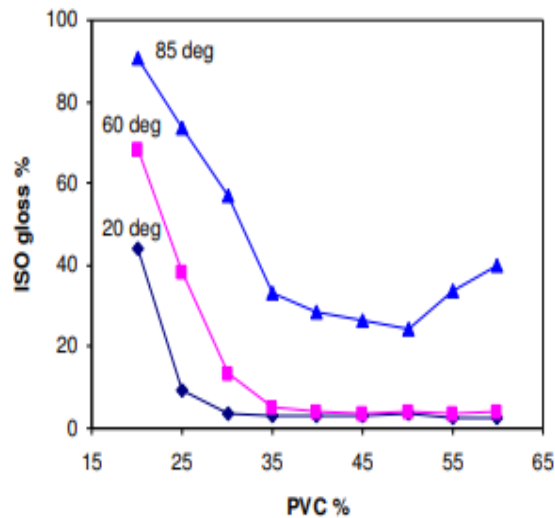


Figure 19: Figure from [62] showing the decrease in gloss as the PVC of titanium white pigment is increased in a latex paint with a vinyl acetate/ethylene copolymer emulsion base. The middle line, with gloss measurements taken with a 60° beam angle (the same angle used in the current study) align well with the data shown in **Figure 18**.

The lack of binder in high PVC paint films also influences T_2 . As described above, the magnitude of T_2 corresponds to the rigidity of a material. [41] Since unpigmented acrylic emulsion paint films remain pliable after drying, but films with higher pigment concentrations become brittle and chalky, the T_2 of the paint films is expected to decrease as their PVC increases. This is supported by the single-sided NMR data collected. **Figure 20** shows the changes in the observed T_2 of acrylic emulsion paint films made with four different pigments as the PVC is increased. These T_2 values, tabulated in **Appendix A, Table 3**, were determined using a monoexponential fit of the echo decay trains collected during the CPMG experiments.

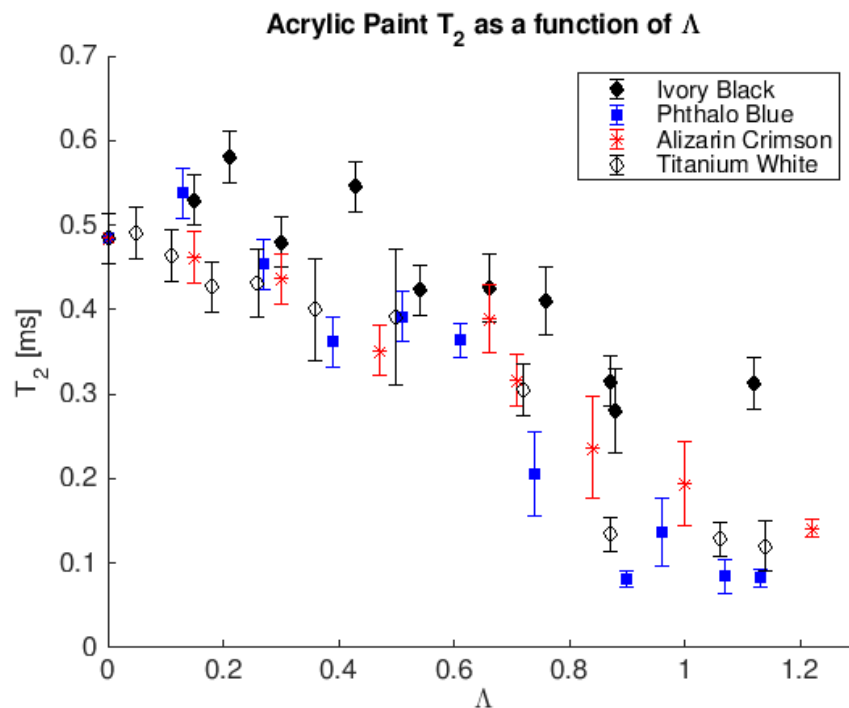


Figure 20: The T_2 relaxation times calculated for paint samples at varying Λ values. These T_2 values were determined using a monoexponential fit of the raw data. The data used for this fit discarded the first two echoes of each echo train decay for all data sets except those for above-CPVC phthalo blue, alizarin crimson, and titanium white samples, which showed no visible decay without the first two echoes. This improved the accuracy of the monoexponential fit, but also removed the possibility of examining a component with a shorter relaxation time.

To further probe the relationship between T_2 and PVC, the raw NMR data was reprocessed using an Inverse Laplace Transform (ILT). This mathematical technique, which converts variables from the one domain to another, in this case the time domain to the ' T_2 domain', is useful in looking at NMR data in studies of complex materials since it can reveal the existence of multiple T_2 values in a sample. [74, 75] ILT analysis of the paint films revealed that some of the samples show two distinct T_2 values that differ by an order of magnitude. Furthermore, it appeared that the proportion of the signal belonging to the larger T_2 decreased with increasing PVC, as can be seen in **Figure 21**.

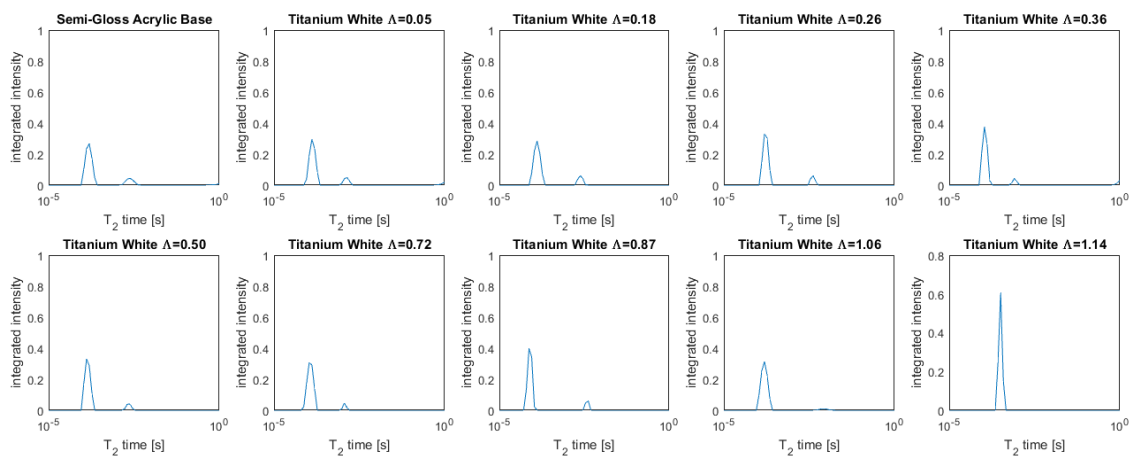


Figure 21: Inverse Laplace Transforms (ILTs) of raw NMR data for titanium white paint samples, arranged in order of increasing Λ value. Each peak on the plot represents a possible T_2 value for the sample, and the peak heights correspond to each T_2 value's contribution to the overall observed signal.

Since ILTs are ill-conditioned and occasionally return ambiguous solutions, [74, 75] the raw NMR data was re-processed with biexponential fits to determine the samples' T_2 values. The biexponential fit was shown to model the echo decays more accurately than the monoexponential fit in samples with a low PVC, confirming the presence of two unique T_2 values in paint films with pigment concentrations up to the CPVC. **Figure 22** shows the changes in both the large and small T_2 values as Λ increases, and numerical results for the exponential T_2 fits are given in **Appendix A, Table 4**. As is evident in **Figure 22**, the small T_2 value remains nearly constant for all samples regardless of pigment type or pigment concentration, whereas the large T_2 value decreases and eventually disappears in samples with a Λ value near and above 1.

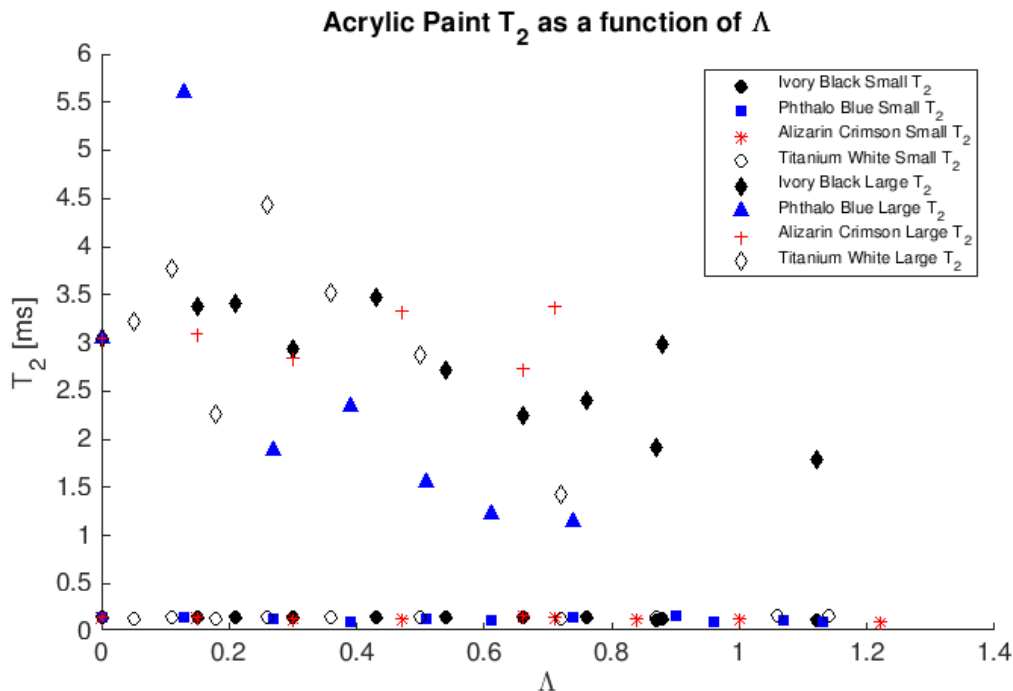


Figure 22: Large and small T_2 values of all samples vs. Λ . The small T_2 value remains nearly constant for all samples regardless of pigment type or pigment concentration, whereas the large T_2 value decreases and eventually disappears in all samples with a Λ value near and above 1, except for those produced with ivory black pigment.

Previous single-sided NMR research has described polymers that exhibit multiple T_2 values. NMR studies of materials like polyethylene (PE), for example, give results analogous to those obtained in this study. [44] PE, which is used in pipes, is a semicrystalline polymer that has areas of ordered and disordered polymer chains making up crystalline and amorphous regions that have, respectively, a smaller and a larger T_2 . However, PE is classified as a hard polymer and the polymers used in acrylic emulsion paint are much softer so they should not have a crystalline phase; a cured acrylic film is composed of amorphous polymer chain tangles. [64-70] Studies of the glass transitions of

paints and other materials in which particulate matter is added to a polymer matrix have concluded that in this type of system, however, the polymer can be described similarly to semicrystalline polymers like PE. Polymer binder chains adsorbed to particles, with limited molecular mobility, are considered a crystalline “interphase” between the particles and the amorphous bulk binder. [56, 72, 77]

It therefore stands to reason that the small T_2 observed in the single sided NMR measurements corresponds to adsorbed binder and the large T_2 to the bulk binder: “free” or “bulk” polymer should have a larger T_2 than crosslinked polymer or polymer adsorbed onto pigment particles, since adsorbed or crosslinked molecules experience a limited amount of motion. [40] This interpretation, though, at first seems contradicted by the fact that the unpigmented acrylic base has two T_2 values. However, the SEM data in **Figure 23** shows that the acrylic base itself contains silicate particulate matter, probably glass or pure silica added as a thickener or extender. [2, 3] Therefore the small T_2 value measured for the base is assumed to come from binder adsorbed to these silica particles.

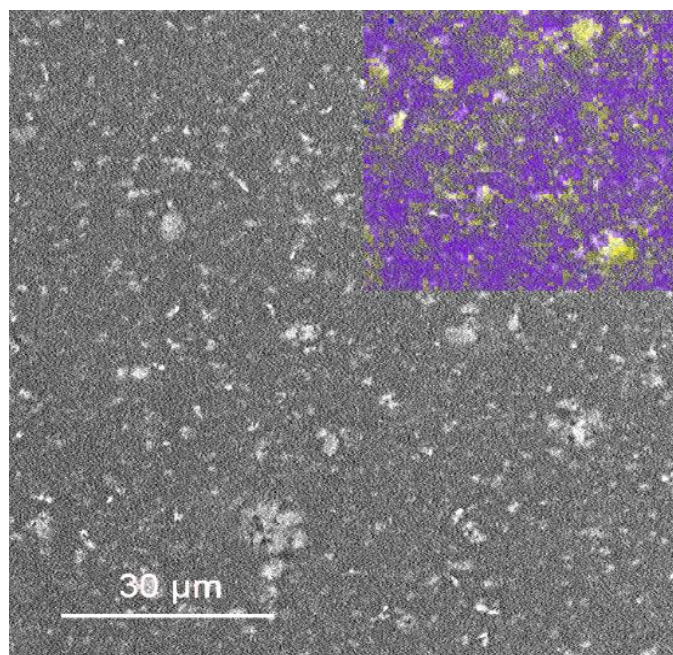


Figure 23: SEM image of unpigmented Semi-Gloss acrylic base showing silica particles, with an EDS elemental map overlaid. Yellow areas indicate the presence of silicon, and purple regions indicate carbon.

To gain a clearer idea of the T_2 trends, the normalized amplitudes of the small and large T_2 values were calculated by dividing each T_2 value's amplitude by the sum of the two components' amplitudes. In this way, the contribution of the small and large T_2 values to the overall observed signal for each sample could be determined. As shown in **Figure 24**, the change observed in the normalized amplitudes of the small T_2 values displays a nearly linear relationship with the change in Λ before reaching a maximum of 1 near the CPVC for most of the pigments studied, with the exception of ivory black. The maximum of 1 corresponds to the point where the small T_2 value accounts for the entirety of the observed signal. This shows the increasing abundance of the samples' small T_2 with increased Λ , and therefore that more binder is adsorbed to pigment particles, as expected.

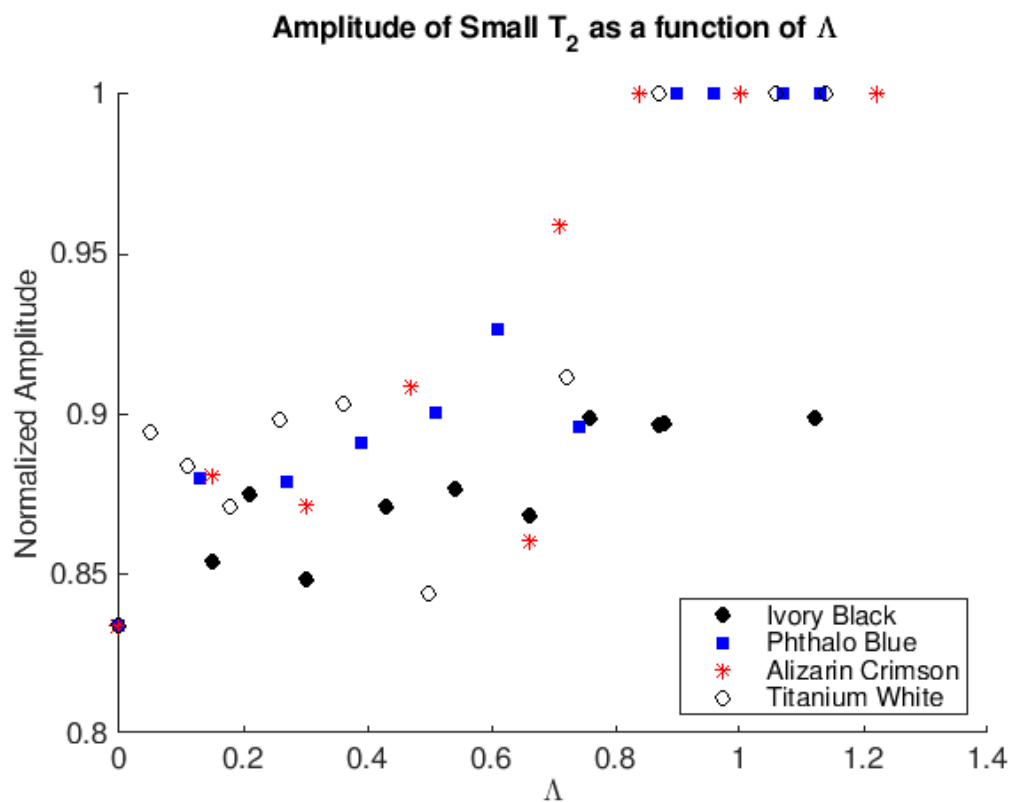


Figure 24: Normalized amplitude of the small T_2 value as a function of Λ , showing the contribution of the small T_2 value to the overall observed signal. The amplitude of the small T_2 value increases as Λ increases until it becomes the only T_2 value observed for high PVC samples of alizarin crimson, phthalo blue, and titanium white samples. The outliers in titanium white ($\Lambda=0.50$) and alizarin crimson ($\Lambda=0.66$) are caused by problems with the positioning of the sample.

The slopes for the fits for each pigment are different however, and may be indicative of particle size; this appears to be upheld by the SEM data in **Figure 25**, in which the sizes of the pigment particles can be seen: ivory black pigment, whose grains have an average size of 10 μm , for example, has an overall lower incidence of the smaller T_2 than titanium white, whose grains have an average size of 0.5 μm . [78, 79] phthalo blue, which has particles with a diameter of between 100 and 200 nm, the smallest of any of the pigments used in this study, seems to have the most drastic effect on the small T_2 value's amplitude. If the particles are smaller, the pigment has a larger surface area and more binder can adsorb, resulting in the smaller T_2 comprising a larger proportion of the overall signal. Therefore, pigments with larger surface area or smaller particle size will have a greater effect on the physical properties of a paint film as pigment concentration increases.

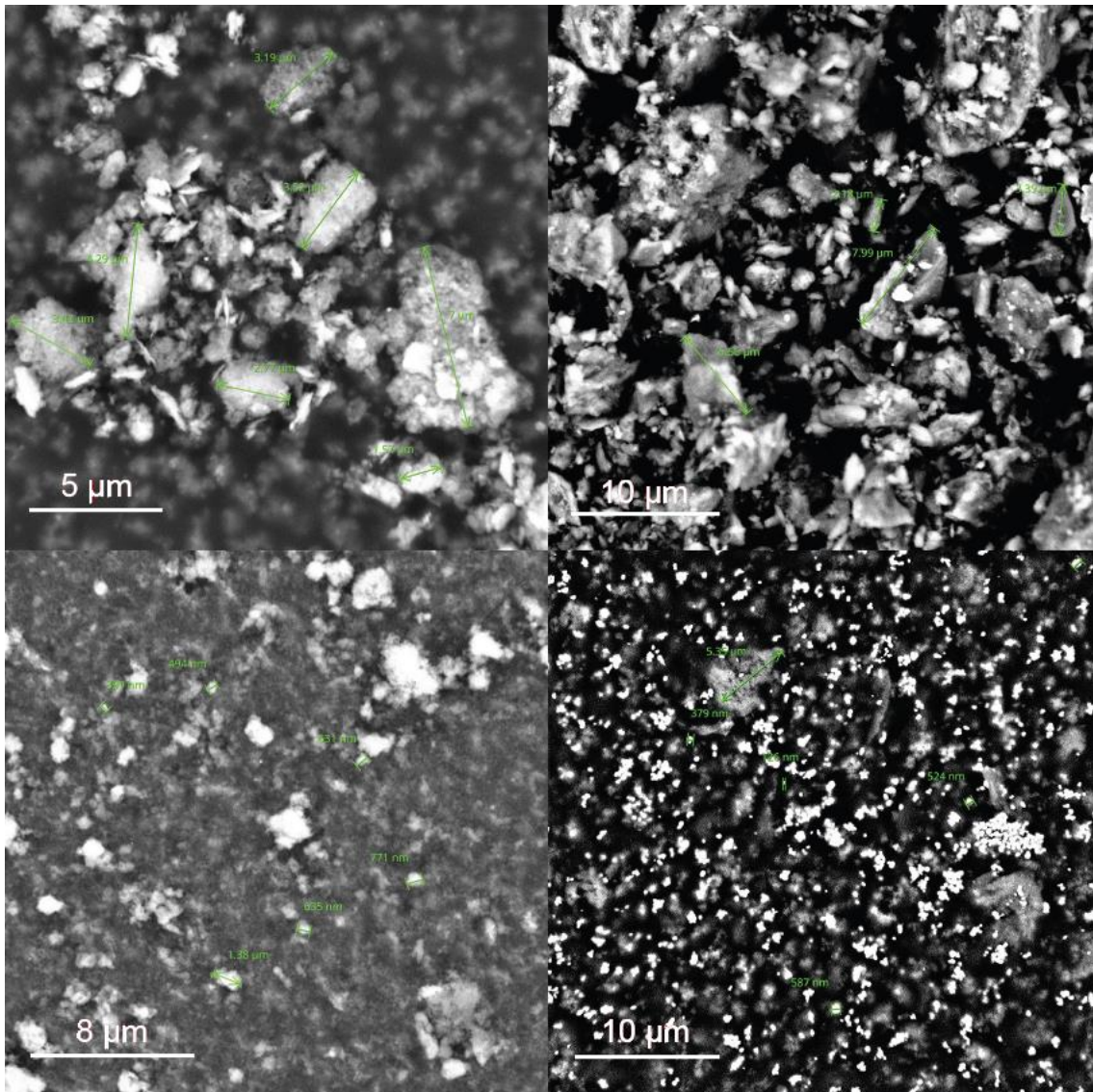


Figure 25: SEM images of the four pigments used for making paints in this study. Clockwise from top left, alizarin crimson (dry), ivory black (dry), titanium white (in semi-gloss acrylic base), and phthalo blue (dry). On average, ivory black particles are largest in size, close to ten microns, followed closely by alizarin crimson particles. Phthalo blue and titanium white have much smaller particles, usually less than one micron in diameter.

Particle size cannot be the only factor affecting the percentage of small T_2 , though, since if that were the case an increase in alizarin crimson pigment particles (average diameter 1-2 μm) should cause the amount of small T_2 to increase more slowly than an increase in titanium white particles (average diameter 0.2 μm). Since this does not seem to be the case, it is likely that the structure of the pigment also influences its effect on T_2 . Organic pigments, like alizarin crimson and phthalo blue, may adsorb more of the hydrophobic polymer chains more closely than inorganic, hydrophilic pigments like titanium white. This would also explain why ivory black is the only pigment which still displays a large T_2 value even in paint films above the CPVC: since it has very large particles and is inorganic, it adsorbs a relatively small amount of acrylic binder.

Data collected for acrylic binder without silica extender, however, points toward an even more complex relationship between polymer matrix and added particles. As discussed earlier, films of unpigmented semi-gloss acrylic binder (which contains silica particles with an average diameter of about 5 μm to reduce gloss and increase opacity and thickness) display two T_2 values, one larger, one smaller. Films of unpigmented regular gloss acrylic base, which contains no particulates, still show two T_2 values, but, although the smaller T_2 of the gloss base is similar to the smaller T_2 of the semi-gloss base, the larger T_2 of the semi-gloss base is more than three times the length of the large T_2 of the gloss base. After adding pigment to the regular gloss base, the larger T_2 increases to approximately the same length as the large T_2 of semi-gloss films with the same level of pigmentation, as shown in **Figure 26**. The numerical data shown on this chart is also listed in **Table 5**.

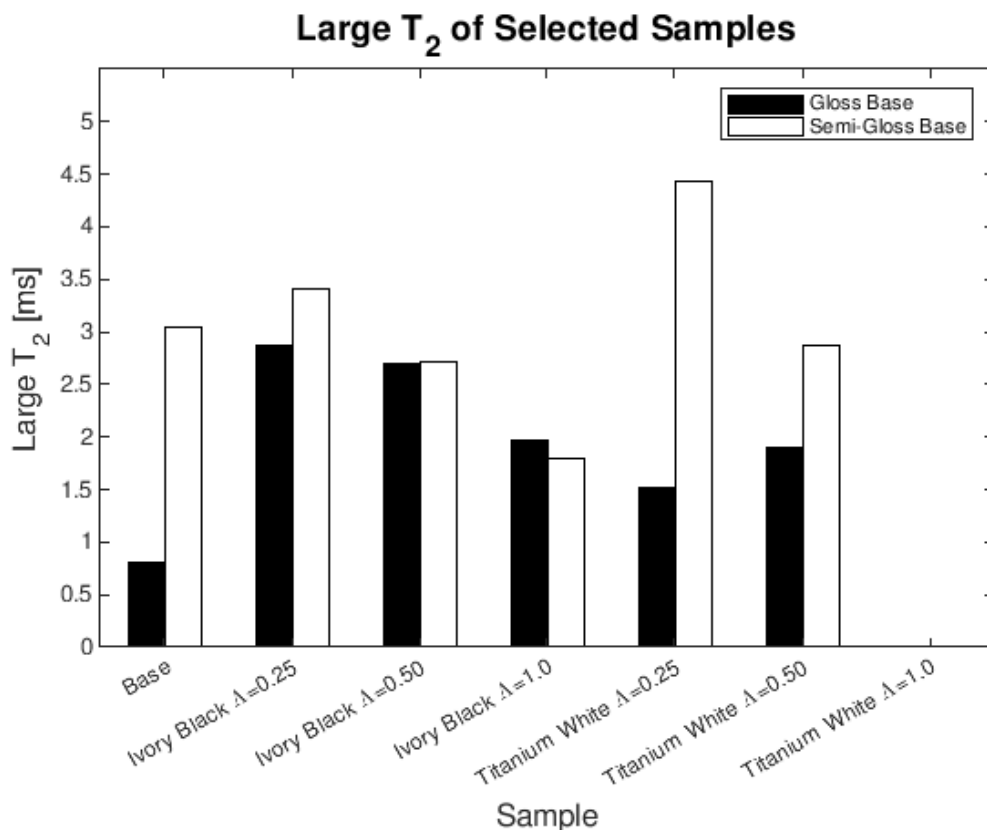


Figure 26: Large T_2 values of ivory black and titanium white samples at different levels of pigmentation and formulated with different acrylic binders. The large T_2 seems to increase as a small amount of particles added (note the large difference in T_2 between the two bases, the gloss base which has no added particles and the semi-gloss base which contains silica filler) and then decrease again with higher amounts of added particles. The apparent absence of data for titanium white at a concentration of $\Lambda=1.0$ is intentional, since these samples only display a small T_2 value.

This result seems to show that film T_2 actually increases as small amounts of particles are introduced, before dropping with the addition of more particles as observed in the films of pigmented semi-gloss binder previously studied. An explanation of this phenomenon may be that adding a small amount of particulate matter disorders the polymer matrix enough to increase the T_2 , without adsorbing enough polymer to decrease T_2 by limiting molecular motion. This disorder is likely to take the form of increased local free volume, or cavities in the polymer film. [41] The local free volume in polymer films with added particles has previously been studied using Positron Annihilation Lifetime Spectroscopy (PALS), and has been shown to increase in both size and frequency with increasing percentage by weight of silica particles added to a polymer film. [80] These cavities form when polymer chain packing is disrupted, especially by an added hydrophilic filler which cannot easily adsorb the hydrophobic polymer chains. In the areas of the film where the local free volume increases, the polymer chains have a higher mobility than adsorbed polymer chains or the densely packed chains in bulk polymer, increasing the observed T_2 value.

Chapter 6: Conclusions

Complementary single-sided NMR and SEM-EDS data have helped to improve understanding of the formation of acrylic paint films. Comparing these measurements shows that as pigment concentration is increased in paints, the paint films' relaxation time changes. The majority of the paint films, especially those with a PVC lower than the CPVC, exhibit two separate T_2 values, a large and a small, that correspond to different environments in the polymer binder. Films with a high PVC have a significantly lower occurrence of a long relaxation time than low PVC films since the amount of binder adsorbed to pigment particles increases with increasing PVC, restricting molecular motion. Pigments with a larger surface area or smaller particle size may have a greater effect on physical properties since more binder can adsorb to them. Additionally, data collected for acrylic binder without silica extender point towards an even more complex relationship between polymer matrix and added particles, in which a very small amount of added particles (pigment or extender, less than 25% volume concentration) increases polymer mobility by creating open spaces in the film.

The data for the two acrylic binders may not be fully comparable however, because it is not certain that the inclusion of silica extender is the only difference between them. This is the only difference listed in the manufacturer's product documentation; however, their ingredient information is somewhat vague for proprietary reasons, and the discrepancy in the large T_2 for the two bases may in fact be a result of polymer interactions with another component of the paint, such as a different type of surfactant. It would be beneficial to further study the makeup of the acrylic bases with a method such

as pyrolysis gas chromatography-mass spectrometry which could help identify the polymer itself, as well as some of the additives. [3]

In addition to conducting a more detailed study of the acrylic bases, it would be interesting to expand the number of pigments used in this research to reinforce the connection between particle size and change in T_2 value. With a larger variety of pigments, it could also be determined whether there are other characteristics besides particle size that have a significant effect on paint T_2 values, such as the chemical composition or dipole moment of the pigment which could influence the strength of the binding between the polymer binder and pigment particles. This research could involve computational modelling of the paint system in addition to single-sided NMR measurements of paint films to facilitate interpretation of results.

Another avenue of related research aligns with a different project currently active in our lab, which is investigating the ingress of solvents into paint films during conservation and cleaning efforts. This study uses single-sided NMR to compare the effects of different solvent application methods on identically pigmented films of commercially available traditional and water mixable artists' oil paints. Extending this project to include analysis of solvent ingress into films with varying levels of pigmentation could provide valuable information for conservators of acrylic artwork who need to make decisions about which solvents and solvent application methods to use for cleaning a painting.

Appendix A: Data Tables

Table 1: Pigment Characteristics. All information is available on the Kremer Pigmente website in MSDSs and Pigments Details documents [78, 79, 81, 82] except for the density of Ivory Black pigment and the oil absorption of Alizarin Crimson and Phthalo Blue, which are from [73]). CPVCs were calculated using **Equation 3.2**.

Pigment Name	Kremer Product #	Color Index Name	Color Index #	Oil Absorption	Density (g/cm³)	CPVC Acrylic	CPVC Linseed Oil
Alizarin Crimson	23610	PR 83	58000	76g/100g	1.7	45.99%	41.98%
Ivory Black	47200	PBk 9	77267	60g/100g	2.29	44.46%	40.49%
Phthalo Blue	23060	PB 15:3	74160	70g/100g	1.6	49.55%	45.50%
Titanium White (rutile)	46200	PW 6	77891	20g/100g	4.23	56.53%	52.50%

Table 2: Sample PVCs and Λ values

Semi-Gloss Base							
Alizarin Crimson		Ivory Black		Phthalo Blue		Titanium White	
PVC	Λ	PVC	Λ	PVC	Λ	PVC	Λ
6.84%	0.15	6.61%	0.15	6.32%	0.13	2.87%	0.05
13.92%	0.30	9.24%	0.21	13.20%	0.27	6.11%	0.11
21.80%	0.47	13.41%	0.30	19.11%	0.39	10.01%	0.18
30.14%	0.66	19.07%	0.43	25.16%	0.51	14.78%	0.26
32.77%	0.71	23.90%	0.54	30.46%	0.61	20.63%	0.36
38.82%	0.84	29.40%	0.66	36.72%	0.74	28.02%	0.50
45.82%	1.00	33.61%	0.76	44.74%	0.90	40.56%	0.72
55.89%	1.22	38.68%	0.87	47.81%	0.96	49.43%	0.87
		39.15%	0.88	52.92%	1.07	60.12%	1.06
		49.91%	1.12	56.15%	1.13	64.44%	1.14

Regular Gel Base			
Ivory Black		Titanium White	
PVC	Λ	PVC	Λ
11.21%	0.25	14.76%	0.26
23.05%	0.52	28.06%	0.50
45.46%	1.02	56.44%	1.00

Table 3: T_2 data for paint films made with Golden Semi-Gloss Regular Gel Base, calculated using a monoexponential fit and ignoring the first two echoes in the decay, except where noted.

	PVC	Λ	T2 (ms)	T2 Uncert. (ms)	Comments
Base	0.00%	0	0.48	0.04	
Ivory Black	6.61%	0.15	0.53	0.03	
	9.24%	0.21	0.58	0.03	
	13.41%	0.30	0.48	0.03	
	19.07%	0.43	0.55	0.03	
	23.90%	0.54	0.42	0.03	
	29.40%	0.66	0.43	0.04	
	33.61%	0.76	0.41	0.04	
	38.68%	0.87	0.32	0.03	
	39.15%	0.88	0.28	0.05	
	49.91%	1.12	0.31	0.03	
Phthalo Blue	6.32%	0.13	0.54	0.03	
	13.20%	0.27	0.45	0.03	
	19.11%	0.39	0.36	0.03	
	25.16%	0.51	0.39	0.03	
	30.46%	0.61	0.36	0.02	
	36.72%	0.74	0.21	0.05	
	44.74%	0.90	0.08	0.01	
	47.81%	0.96	0.14	0.04	
	52.92%	1.07	0.08	0.02	No echoes omitted
	56.15%	1.13	0.08	0.01	No echoes omitted
Alizarin Crimson	6.84%	0.15	0.46	0.03	
	13.92%	0.30	0.44	0.03	
	21.80%	0.47	0.35	0.03	
	30.14%	0.66	0.39	0.04	
	32.77%	0.71	0.32	0.03	
	38.82%	0.84	0.24	0.06	
	45.82%	1.00	0.19	0.05	
	55.89%	1.22	0.14	0.01	No echoes omitted
Titanium White	2.87%	0.05	0.49	0.03	
	6.11%	0.11	0.46	0.03	
	10.01%	0.18	0.43	0.03	
	14.78%	0.26	0.43	0.04	
	20.63%	0.36	0.40	0.06	
	28.02%	0.50	0.39	0.08	
	40.56%	0.72	0.31	0.03	
	49.43%	0.87	0.13	0.02	No echoes omitted
	60.12%	1.06	0.13	0.06	No echoes omitted
	64.44%	1.14	0.12	0.03	No echoes omitted

Table 4: T_2 data for paint films made with Golden Semi-Gloss Regular Gel Base, calculated using a biexponential fit with no echoes omitted where required, and a mono exponential fit where the biexponential fit returned identical T21 and T22 values.

	PVC	Λ	Monofit	Bifit			
			T2 (ms)	T2 (higher %)	Amplitude	T2 (lower %)	Amplitude
Base	0.00%	0.00		0.1558	37.550	3.050	7.476
Ivory Black	6.61%	0.15		0.1461	39.080	3.384	6.670
	9.24%	0.21		0.1512	25.300	3.406	3.606
	13.41%	0.30		0.1494	24.450	2.936	4.362
	19.07%	0.43		0.1558	16.690	3.475	2.472
	23.90%	0.54		0.1463	22.080	2.710	3.112
	29.40%	0.66		0.1545	16.080	2.238	2.434
	33.61%	0.76		0.1494	22.720	2.394	2.560
	38.68%	0.87		0.1209	14.460	1.921	1.666
	39.15%	0.88		0.1332	13.580	2.977	1.555
	49.91%	1.12		0.1130	17.800	1.793	1.997
Phthalo Blue	6.32%	0.13		0.1497	4.354	5.604	0.594
	13.20%	0.27		0.1405	32.170	1.885	4.400
	19.11%	0.39		0.0983	10.290	2.331	1.256
	25.16%	0.51		0.1324	22.680	1.544	2.509
	30.46%	0.61		0.1222	13.950	1.222	1.107
	36.72%	0.74		0.1434	14.190	1.140	1.657
	44.74%	0.90	0.1575				
	47.81%	0.96	0.1084				
	52.92%	1.07	0.1103				
	56.15%	1.13	0.0951				
Alizarin Crimson	6.84%	0.15		0.1513	41.830	3.100	5.648
	13.92%	0.30		0.1394	23.670	2.850	3.478
	21.80%	0.47		0.1379	40.560	3.337	4.055
	30.14%	0.66		0.1590	11.370	2.731	1.845
	32.77%	0.71		0.1515	12.670	3.375	0.538
	38.82%	0.84	0.1294				
	45.82%	1.00	0.1341				
	55.89%	1.22	0.1094				
Titanium White	2.87%	0.05		0.1398	43.330	3.225	5.107
	6.11%	0.11		0.1468	37.260	3.771	4.878
	10.01%	0.18		0.1308	26.080	2.257	3.859
	14.78%	0.26		0.1544	36.410	4.439	4.114
	20.63%	0.36		0.1489	21.710	3.525	2.325
	28.02%	0.50		0.1533	27.320	2.872	5.058
	40.56%	0.72		0.1320	36.560	1.432	3.537
	49.43%	0.87	0.1480				
	60.12%	1.06	0.1608				
	64.44%	1.14	0.1674				

Table 5: T_2 data for Ivory Black and Titanium White paint films made with Golden Regular Gel Gloss Base (top) and Golden Semi-Gloss Regular Gel Base (bottom). No large T_2 is given for paint films with a high concentration of Titanium White pigment since the echo train decay for those concentrations is best modelled using a monoexponential fit; a biexponential fit of that data shows two identical T_2 values.

		Λ	Small T_2	Amplitude	Large T_2	Amplitude
	Gloss Base	Base	0.00	0.1350	23.54	0.8043
Ivory Black		0.25	0.1600	26.76	2.866	4.063
		0.50	0.1566	26.39	2.702	6.887
		1.00	0.1801	14.56	1.974	2.510
Titanium White		0.25	0.1581	22.43	1.513	2.397
		0.50	0.1621	34.40	1.899	3.065
		1.00	0.1616		-	

		Λ	Small T_2	Amplitude	Large T_2	Amplitude
	Semi-Gloss Base	Base	0.00	0.1558	37.550	3.050
Ivory Black		0.21	0.1512	25.300	3.406	3.606
		0.54	0.1463	22.080	2.710	3.112
		1.12	0.1130	17.800	1.793	1.997
Titanium White		0.26	0.1544	36.410	4.439	4.114
		0.50	0.1533	27.320	2.872	5.058
		1.14	0.1674		-	

Appendix B: Experimental Parameters

Profile:

B_1 Frequency (MHz)	19.27
90° Pulse Amplitude (dB)	-10
180° Pulse Amplitude (dB)	-4
Pulse Length (μ s)	2.75
Resolution (μ m)	200
Repetition Time (μ s)	500
Number of Scans	256
Number of Echoes	64
Initial Depth (μ m)	1100
Final Depth (μ m)	500
Step Size (μ m)	-20

CPMG:

B_1 Frequency (MHz)	19.27
90° Pulse Amplitude (dB)	-10
180° Pulse Amplitude (dB)	-4
Pulse Length (μ s)	2.75
Resolution (μ m)	200
Repetition Time (μ s)	500
Number of Scans	256
Number of Echoes	64
Number of Complex Points	64
Dwell Time (μ s)	0.5

Debugger Script:

The parameters adjusted for each sample are indicated by ‘%’.

```
procedure (CPMGBD)
# Cache macros
  cd("$appdir$\Macros\Kea-NMR")
  cachemacro("CPMG.mac", "local")
  cd("$appdir$\Macros\Kea-Core")
  cachemacro("keaCtrl.mac", "local")
  cachemacro("keaRun.mac", "local")
  cachemacro("keaPlot.mac", "local")
  cachemacro("keaFiles.mac", "local")
  cd("$appdir$\Macros\NMR-MOUSE")
  cachemacro("Service2.mac", "local")
  cacheproc("true")
# Set up gui par
  guipar = ["90Amplitude = -10",
            "180Amplitude = -4",
            "accumulate = \"yes\"",
            "acqTime = 0.032",
            "alpha = 1e10",
            "autoPhase = \"yes\"",
            "b1Freq = 19.21",
            "bandwidth = 2000",
            "dataDirectory = \"Z:\Data\MTR\Paint\"", % Change file location
            "dummies = 0",
            "dummyEchoes = 0",
            "dwellTime = 0.5",
            "echoShift = 0",
            "echoTime = 60",
            "expName = \"TitaniumWhite49.43Slide3new\"", % Change experiment name
            "expNr = 0",
            "filter = \"no\"",
            "filterType = \"sinebellsquared\"",
            "fitType = \"nnls\"",
            "flatFilter = \"no\"",
            "incExpNr = \"yes\"",
            "normalize = \"yes\"",
            "nrEchoes = 64",
            "nrPnts = 64",
            "nrScans = 2048",
            "pulseLength = 2.75",
            "repTime = 500",
            "rxGain = 31",
            "rxPhase = 247",
            "saveData = \"true\"",
            "sumEchoes = \"no\"",
            "timeMag = \"no\"",
            "usePhaseCycle = \"yes\"",
            "x_maximum = 100",
            "x_minimum = 0.2"]
# Run the macro via the backdoor
for(t = 0 to 2)
  guipar = setlistvalue(guiPar, "expNr", "\"$t$")
  CPMG:backdoor(guiPar)
  pause(3)
next(t)
endproc()
```

Appendix C: Abbreviations

CPMG	Carr-Purcell-Meiboom Gill Pulse Sequence
CPVC	Critical Pigment Volume Concentration
EA	Ethyl Acrylate
EDS	Energy Dispersive Spectrometry
FID	Free Induction Decay
FTIR	Fourier Transform Infrared Spectroscopy
GU	Gloss Units
ILT	Inverse Laplace Transform
MMA	Methyl Methacrylate
MOUSE	Mobile Universal Surface Explorer
MS	Mass Spectrometry
nBA	n-Butyl Acrylate
NMR	Nuclear Magnetic Resonance (Spectroscopy)
PE	Polyethylene
PVC	Pigment Volume Concentration
RF	Radiofrequency
SEM	Scanning Electron Microscopy

Appendix D: Acquisition Parameter Terms

1. 90° and 180° Amplitude (dB): The power of the applied 90° on-resonance excitation pulse and 180° refocusing pulse
2. Pulse Length (μs): The length of application for the 90° and 180° pulses; this varies according to the number of spacers inserted into the magnet.
3. Echo time (μs): The time after which each echo is acquired (explained in detail in Chapter 3). The echo time multiplied by the number of echoes is approximately equal to the length of one scan.
4. Repetition Time (ms): The time between the beginning of one scan and the initiation of another scan with a new excitation pulse. The repetition time is the length of an entire scan and can be used to estimate the length of a full CPMG experiment.
5. Number of Scans: The number of repeated pulse sequences in the CPMG experiments. More scans generate a greater amount of signal since more signal amplitudes are added, but also lengthen an experiment.
6. Number of Echoes: The number of echoes obtained during each scan. Samples with short relaxation times require less echoes to capture the full signal decay.
7. Number of Complex Points: The number of digital points collected to construct each echo. The acquisition time for an echo can be calculated by multiplying the number of complex points by the dwell time.
8. Dwell Time (μs): The length of time needed to collect each complex point.
9. Depth (μm): The distance into a sample where the single-sided NMR is acquiring data. The highest point at which the magnet acquires data is given by the initial depth, and the final depth is the point to which the magnet is lowered.

Bibliography:

- [1] Willneff, E. A.; Schroeder, S. L.; Ormsby, B. A. Spectroscopic techniques and the conservation of artists' acrylic emulsion paints. *Heritage Sci.* **2014**, *2*(1), 25-34.
- [2] Croll, S. Overview of developments in the paint industry since 1930. *Modern Paints Uncovered: Proceedings from the Modern Paints Uncovered Symposium*, Getty Publications: Los Angeles, 2007; pp. 17–29.
- [3] Learner, T. J. Modern paints: Uncovering the choices. *Modern Paints Uncovered: Proceedings from the Modern Paints Uncovered Symposium*, Getty Publications: Los Angeles, 2007; pp. 3–16.
- [4] Nakayama, Y. Polymer blend systems for water-borne paints. *Prog. Org. Coat.* **1998**, *33*(2), 108-116.
- [5] Jablonski, E.; Learner, T.; Golden, M. Conservation concerns for acrylic emulsion paints: a literature review. *Stud. Conserv.* **2003**, *48*(Suppl. 1), 3-12.
- [6] Dillon, C.E.; Lagalante, A.F. Wolbers, R.C. Acrylic emulsion paint films: the effect of solution pH, conductivity, and ionic strength on film swelling and surfactant removal. *Stud. Conserv.* **2014**, *59*(1), 52-62.
- [7] Evanson, K. W.; Thorstenson, T. A.; Urban, M. W. Surface and interfacial FTIR spectroscopic studies of latexes. II. Surfactant-copolymer compatibility and mobility of surfactants. *J. Appl. Polym. Sci.* **1991**, *42*(8), 2297-2307.
- [8] Solbes-Garcia, Á.; Miranda-Vidales, J.M.; Nieto-Villena, A.; Hernandez, L.S.; Narváez, L. Evaluation of the oxalic and tartaric acids as an alternative to citric acid in aqueous cleaning systems for the conservation of contemporary acrylic paintings. *J. Cult. Herit.* **2017**, *25*, 127-134.
- [9] Papiiaka, Z.E.; Andrikopoulos, K.S.; Varella, E.A. Study of the stability of a series of synthetic colorants applied with styrene-acrylic copolymer, widely used in contemporary paintings, concerning the effects of accelerated ageing. *J. Cult. Herit.* **2010**, *11*, 381-391.
- [10] Wang, J.; Xu, H.; Battocchi, D.; Bierwagen, G. The determination of critical pigment volume concentration (CPVC) in organic coatings with fluorescence microscopy. *Prog. Org. Coat.* **2014**, *77*, 2147-2154.

- [11] Spyros, A.; Anglos, D. Studies of organic paint binders by NMR spectroscopy. *Appl. Phys. A*. **2006**, *83*, 705-708.
- [12] Kampasakali, E.; Ormsby, B.; Cosentino, A.; Miliani, C.; Learner, T. A preliminary evaluation of the surfaces of acrylic emulsion paint films and the effects of wet-cleaning treatment by atomic force microscopy (AFM). *Stud. Conserv.* **2011**, *56*, 216-230.
- [13] Nechvilová, K.; Kalendová, A. Properties of organic coatings containing pigments with surface modified with a layer of ZnFe₂O₄. *ASTRJ.* **2015**, *9*(28), 51–55.
- [14] Karakaş, F.; Hassas, B.V.; Çelik, M. Effect of precipitated calcium carbonate additions on waterborne paints at different pigment volume concentrations. *Prog. Org. Coat.* **2015**, *83*, 64-70.
- [15] Karakaş, B.V.; Çelik, M. Mechanism of TiO₂ stabilization by low molecular weight NaPAA in reference to water-borne paint suspensions. *Colloids and Surfaces A: Physicochem. Eng. Aspects.* **2013**, *434*, 185–193.
- [16] Hagan, E.W.S. Thermo-mechanical properties of white oil and acrylic artist paints. *Prog. Org. Coat.* **2017**, *104*, 28-33.
- [17] Ferreira, J.L.; Melo, M.J.; Ramos, A.M. Poly(vinyl acetate) paints in works of art: a photochemical approach. Part 1. *Polym. Degrad. Stab.* **2010**, *95*, 453-461.
- [18] Khorassani, M.; Afshar-Taromi, F.; Mohseni, M.; Pourmahdian, S. The role of auxiliary monomers and emulsifiers on wet scrub resistance of various latex paints at different pigment volume concentrations. *J. Appl. Polym. Sci.* **2009**, *113*, 3264-3268.
- [19] Topçuoğlu, Ö.; Altinkaya, S.A.; Balköse, D. Characterization of waterborne acrylic based paint films and measurement of their water vapor permeabilities. *Prog. Org. Coat.* **2006**, *56*, 269-278.
- [20] Presciutti, F.; Perlo, J.; Casanova, F.; Glöggler, S.; Miliani, C.; Blümich, B.; Brunetti, B. G.; Sgamellotti, A. Noninvasive nuclear magnetic resonance profiling of painting layers. *Appl. Phys. Lett.* **2008**, *93*(3), 033505.
- [21] Casanova, F.; Perlo, J.; Blümich, B. Single-sided NMR. *Single-Sided NMR*, Springer-Verlag: Berlin, 2011; pp. 1–10.

- [22] Del Federico, E.; Centeno, S. A.; Kehlet, C.; Currier, P.; Stockman, D.; Jerschow, A. Unilateral NMR applied to the conservation of works of art. *Anal. Bioanal. Chem.* **2010**, *396*(1), 213–220.
- [23] Blümich, B.; Haber, A.; Casanova, F.; Del Federico, E.; Boardman, V.; Wahl, G.; Stilliano, A.; Isolani, L. Noninvasive depth profiling of walls by portable nuclear magnetic resonance. *Anal. Bioanal. Chem.* **2010**, *397*(7), 3117–3125.
- [24] Haber, A.; Blümich, B.; Souvorova, D.; Del Federico, E. Ancient roman wall paintings mapped nondestructively by portable NMR. *Anal. Bioanal. Chem.* **2011**, *401*(4), 1441–1452.
- [25] Ulrich, K.; Centeno, S.A.; Arslanoglu, J.; Del Federico, E.D. Absorption and diffusion measurements of water in acrylic paint films by single-sided NMR. *Prog. Org. Coat.* **2011**, *71*, 283–289.
- [26] Blümich, B.; Casanova, F.; Perlo, J.; Presciutti, F.; Anselmi, C.; Doherty, B. Noninvasive testing of art and cultural heritage by mobile NMR. *Acc. Chem. Res.* **2010**, *43*(6), 761–770.
- [27] Casieri, C.; Terenzi, C.; De Luca, F. Two-dimensional longitudinal and transverse relaxation time correlation as a low-resolution nuclear magnetic resonance characterization of ancient ceramics. *J. Appl. Phys.* **2009**, *105*(3), 034901.
- [28] Terenzi, C.; Casieri, C.; Felici, A. C.; Piacentini, M.; Vendittelli, M.; De Luca, F. Characterization of elemental and firing-dependent properties of phlegrean ceramics by non-destructive ED-XRF and NMR techniques. *J. Archaeol. Sci.* **2010**, *37*(7), 1403–1412.
- [29] Blümich, B.; Anferova, S.; Sharma, S.; Segre, A.; Federici, C. Degradation of historical paper: nondestructive analysis by the NMR-MOUSE. *J. Magn. Res.* **2003**, *161*(2), 204–209.
- [30] Proietti, N.; Capitani, D.; Pedemonte, E.; Blümich, B.; Segre, A. Monitoring degradation in paper: non-invasive analysis by unilateral NMR. part ii. *J. Magn. Res.* **2004**, *170*(1), 113–120.
- [31] Marigheto, N.; Duarte, S.; Hills, B. NMR relaxation study of avocado quality. *Appl. Magn. Res.* **2005**, *29*(4), 687–701.

- [32] Marigheto, N.; Venturi, L.; Hills, B. Two-dimensional NMR relaxation studies of apple quality. *Postharvest Biol. Technol.* **2008**, *48*(3), 331–340.
- [33] Musse, M.; Cambert, M.; Mariette, F. NMR study of water distribution inside tomato cells: effects of water stress. *Appl. Magn. Res.* **2010**, *38*(4), 455–469.
- [34] Hernández-Sánchez, N.; Hills, B.; Barreiro, P.; Marigheto, N. An NMR study on internal browning in pears. *Postharvest Biol. Technol.* **2007**, *44*(3), 260–270.
- [35] Nordon, A.; McGill, C. A.; Littlejohn, D. Process NMR spectrometry. *Analyst* **2001**, *126*(2), 260–272.
- [36] Mitchell, J.; Gladden, L.; Chandrasekera, T.; Fordham, E. Low-field permanent magnets for industrial process and quality control. *Prog. Nucl. Magn. Reson. Spectrosc.* **2014**, *76*, 1–60.
- [37] Sharma, S.; Casanova, F.; Wache, W.; Segre, A.; Blümich, B. Analysis of historical porous building materials by the NMR-MOUSE. *Magn. Reson. Imaging* **2003**, *21*(3), 249–255.
- [38] Carr, H. Y.; Purcell, E. M. Effects of diffusion on free precession in nuclear magnetic resonance experiments. *Phys. Rev.* **1954**, *94*(3), 630-638.
- [39] Meiboom, S.; Gill, D. Modified spin-echo method for measuring nuclear relaxation times. *Rev. Sci. Instrum.* **1958**, *29*(8), 688–691.
- [40] Bloembergen, N.; Purcell, E. M.; Pound, R. V. Relaxation effects in nuclear magnetic resonance absorption. *Phys. Rev.* **1948**, *73*(7), 679.
- [41] Forsyth, M.; MacFarlane, D.R.; Best, A.; Adebahr, J.; Jacobsson, P.; Hill, A.J. The effect of nano-particle TiO₂ fillers on structure and transport in polymer electrolytes. *Solid State Ionics.* **2002**, *147*, 203-211.
- [42] Solomon, I.; Relaxation processes in a system of two spins *Phys. Rev.* **1955**, *99* (2), 559.
- [43] Levitt, M. H.; *Spin Dynamics*, 2nd ed.; Wiley: Chichester, U.K., 2008; pp. 5-38

- [44] Silverstein, R. M.; Webster, F. X.; Kiemle, D. J.; Bryce, D. L. Proton (^1H) Magnetic Resonance Spectroscopy. *Spectrometric Identification of Organic Compounds*, 8th ed.; Wiley: Hoboken, NJ, 2015; pp. 126-190.
- [45] Eidmann, G.; Savelsberg, R.; Blümmler, P.; Blümich, B. The NMR MOUSE, a mobile universal surface explorer. *J. Magn. Res. Ser. A* **1996**, *122*, 104-109.
- [46] B. Blümich, B.; Blümmler, P.; Eidmann, G.; Guthausen, A.; Haken, R.; Schmitz, U.; Saito, K.; Zimmer, G. The NMR-MOUSE: construction, excitation, and application. *Magn. Reson. Imaging* **1998**, *16*(5/6), 479-484.
- [47] Casanova, F.; Perlo, J. NMR in inhomogeneous fields. *Single-Sided NMR*, Springer-Verlag: Berlin, 2011; pp. 11-56.
- [48] Kolz, J. Applications in material science and cultural heritage. *Single-Sided NMR*, Springer-Verlag: Berlin, 2011; pp. 203–220.
- [49] Udell, N.; Hodgkins, R.E.; Berrie, B.H.; Meldrum, T.; Physical and chemical properties of traditional and water-mixable oil paints assessed using single-sided NMR. *Microchem. J.* **2017**, *133*, 31-36.
- [50] Hahn, E. L. Spin Echoes. *Phys. Rev.* **1950**, *80*(4), 580-594.
- [51] Dollemore, D. Acrylic Emulsion Technology: From plastics to paints it changed our world. *American Chemical Society National Historic Chemical Landmarks, Acrylic Emulsion Technology*. September 15, 2008. <http://www.acs.org/content/acs/en/education/whatischemistry/landmarks/acrylicemulsion.html> (accessed February 18, 2018).
- [52] Conn, W. R.; Kine, B. B.; Prentiss, W. C. (of Rohm & Haas Co. Inc.) Aqueous paint bases and water-based paints and process for preparing them. U.S. Patent 2795564A, May 13, 1953.
- [53] Smith, W. V. The Kinetics of Styrene Emulsion Polymerization. *J. Am. Chem. Soc.* **1948**, *70*(11), 3695–3702.
- [54] Bierwagen, G. CPVC calculations. *J. Paint Technol.* **1972**, *44*(574), 46-55.
- [55] Perera, D. Y. Effect of pigmentation on organic coating characteristics. *Prog. Org. Coat.* **2004**, *50*(4), 247–262.

- [56] Uemoto, K.L.; Agopyan, V.; Vittorino, F. Concrete protection using acrylic latex paints: effect of the pigment volume content on water permeability. *Mater. Struct.* **2001**, *34*, 172-177.
- [57] Asbek, W.K.; Van Loo, M. Critical Pigment Volume Relationships. *Ind. Eng. Chem.* **1949**, *41*(7), 1470-1475.
- [58] Floyd, F.L.; Holsworth, R.M. CPVC as a point of phase inversion in latex paints. *J. Coat. Technol.* **1992**, *64*(806), 65-69.
- [59] Liu, F.; Chou, K.; Determining critical ceramic powder volume concentration from viscosity measurements. *Ceram. Int.* **2000**, *26*, 159-164.
- [60] Bierwagen, G.; Hay, T. The reduced pigment volume concentration as an important parameter in interpreting and predicting the properties of organic coatings. *Prog. Org. Coat.* **1975**, *3*(4), 281-303.
- [61] Brown, R.F.G.; Carr, C.; Taylor, M.E. Effect of pigment volume concentration and latex particle size on pigment distribution. *Prog. Org. Coat.* **1997**, *30*, 185-194.
- [62] Elton, N.; Legrix, A. Reflectometry of drying latex paint. *J. Coat. Technol. Res.* **2014**, *11*(2), 185-197.
- [63] Keddie, J.L.; Meredith, P.; Jones, R.A.L.; Donald, A.M. Kinetics of film formation in acrylic latices studied with multiple-angle-of-incidence ellipsometry and environmental SEM. *Macromolecules.* **1995**, *28*, 2673-2682.
- [64] Keddie, J.L.; Meredith, P.; Jones, R.A.L.; Donald, A.M. Film formation of acrylic latices with varying concentrations of non-film-forming latex particles. *Langmuir* **1996**, *12*, 3793-3801.
- [65] Alsoy, S.; Duda, L. Modeling of multicomponent drying of polymer films. *AIChE J.* **1999**, *45*, 896-905.
- [66] Boczar, E.M.; Dionne, C.; Fu, Z.; Kirk, A.B.; Leake, P.M.; Koller, A.D. Spectroscopic studies of polymer interdiffusion during film formation. *Macromolecules.* **1993**, *26*, 5772-5781.
- [67] Winnik, M.A. Latex film formation. *Curr. Opin. Colloid Interface Sci.* **1997**, *2*, 192-199.

- [68] McDonald, P. J.; Keddie, J. L. Watching paint dry: Magnetic resonance imaging of soft condensed matter. *Europhys. News* **2002**, *33*(2), 48–51.
- [69] Kim, K. D.; Sperling, L.; Klein, A.; Hammouda, B. Reptation time, temperature, and cosurfactant effects on the molecular interdiffusion rate during polystyrene latex film formation. *Macromolecules* **1994**, *27*(23), 6841–6850.
- [70] Townsend, M. Investigating the drying process of acrylic color and gel medium. *Just Paint*. September 1, 2012. <http://www.justpaint.org/investigating-the-drying-process-of-acrylic-color-and-gel-medium/> (accessed January 15, 2018).
- [71] Erich, S.J.F.; Huinink, H.P.; Adan, O.C.G.; Laven, J.; Esteves, A.C. The influence of the pigment volume concentration on the curing of alkyd coatings: A 1D MRI depth profiling study. *Prog. Org. Coat.* **2008**, *63*, 399-404.
- [72] Landry, C.J.T.; Coltrain, B.K.; Landry, M.R.; Fitzgerald, J.J.; Long, V.K. Poly(vinyl acetate)/Silica Filled Materials: Material Properties of in Situ vs Fumed Silica Particles. *Macromolecules*. **1993**, *26*, 3702-3712.
- [73] Mayer, R.; *The Artist's Handbook of Materials and Techniques*, 5th ed.; Viking: New York, New York, 1981.
- [74] Lee, J. H.; Labadie, C.; Springer Jr, C. S.; Harbison, G. S. Two-dimensional inverse laplace transform NMR: altered relaxation times allow detection of exchange correlation. *J. Am. Chem. Soc.* **1993**, *115*(17), 7761–7764.
- [75] Hürlimann, M. D. Ex situ measurement of one-and two-dimensional distribution functions. *Single-Sided NMR*, Springer-Verlag: Berlin, 2011; pp. 57–85.
- [76] Simpson, L. Factors controlling gloss of paint films. *Prog. Org. Coat.* **1978**, *6*(1), 1–30.
- [77] Theocaris, P.; Spathis, G. Glass-transition behavior of particle composites modeled on the concept of interphase. *J. Appl. Polym. Sci.* **1982**, *27*(8), 3019–3025.
- [78] Titanium White Rutile, Product Number 46200, Specification Sheet; Kremer Pigmente GmbH & Co., Aichstetten, Germany.
- [79] Ivory Black, Product Number 47200, Specification Sheet; Kremer Pigmente GmbH & Co., Aichstetten Germany.

[80] Winberg, P.; DeSitter, K.; Dotremont, C.; Mullens, S.; Vankelecom, I. F. J.; Maurer, F. H. J. Free Volume and Interstitial Mesopores in Silica Filled Poly (1-trimethylsilyl-1-propyne) Nanocomposites. *Macromolecules* **2005**, *38*, 3776-3782

[81] *Alizarine Crimson Dark*; MSDS No. 23610; Kremer Pigmente GmbH & Co. KG: Aichstetten, Germany, May 20, 2015.

[82] Phthalo Blue Royal Blue, Product Number 23060, Specification Sheet; Kremer Pigmente GmbH & Co., Aichstetten Germany.